Finite element implementation of Field Crack Mechanics for brittle and ductile fracture

BVSS Bharadwaja[a], Alankar Alankar[a,*]

[a]*Department of Mechanical Engineering, Indian Institute of Technology Bombay, Powai, Mumbai–400076, India*

Abstract

In this work, a Finite Element (FE) implementation of a Field Crack Mechanics (FCM) model is presented for the first time. The implementation includes general boundary conditions and application to bulk plasticity as well. The current numerical investigation adopts the standard Galerkin finite element formulation to solve the equation of linear momentum balance and finite difference framework for crack evolution. Our preliminary investigation includes the modes-I and II loading conditions, where their respective normal stress fields are compared against their analytical counterparts. The fundamental questions in classical fracture mechanics, e.g. the existence of threshold stress for the crack to move, and various stages associated with the crack propagation are investigated. Additionally, this study explores two distinct strain energy functions based on the crack surface normal and hydrostatic deviatoric energy split. Crack irreversibility is a natural phenomenon in the FCM model, and it does not require satisfying any extra irreversibility constraints. The model shows good agreement against literature and analytical framework. The current FCM implementation also recovers the basic notion of fracture propagation which satisfies both energy and stress criterion. The study also explores the crack motion under the effect of plasticity in ductile materials. The results thus obtained for both brittle and ductile fracture cases are consistent with the predictions of classical fracture mechanics. The current implementation of the FCM effectively demonstrates stable crack propagation, eliminating the requirement for surfing boundary conditions.

Keywords: Fracture mechanics, field–crack mechanics, continuum mechanics, finite element modeling

1. Introduction

Fracture is a nearly inevitable phenomenon that may occur for various reasons, such as defects arising during manufacturing, inherent defects in materials, environmental conditions, and prevailing conditions during operation. Therefore, studying complex failure

*Corresponding author, Tel.: +91-9769415356, Fax: +91-22-25726875

Email addresses: bvss89@gmail.com (BVSS Bharadwaja), alankar.alankar@iitb.ac.in (Alankar Alankar)

mechanisms associated with crack propagation in solids is important for durability assessment. The pioneering work of Griffith [1] based on simple thermodynamic principles laid the foundation for fracture mechanics. To solve various initial/boundary value problems in fracture mechanics, numerous computational techniques/models are available in the literature. As mentioned in [2, 3], the main distinguishing feature of the FCM model when compared to the existing models is the vectorial representation of the crack tip field that enables the model to spontaneously capture the crack propagation direction. Furthermore, as observed in [2], the specific advantage of a crack tip field lies in the fact that, regardless of the energy or stress levels, crack evolution exclusively occurs in the presence of crack tip fields. In the present work, a computational framework of a partial differential equation (PDE) based fracture model, field crack mechanics [2] is presented.

Using the FCM model, the present study explores the critical features in crack propagation, such as stable and unstable crack propagations, critical stress, and fracture toughness criterion as suggested by classical fracture mechanics. The framework was first introduced by Acharya [2, 4] in capturing the crack behavior in brittle and ductile solids. Our focus is to develop a computational model related to FCM where the crack region is restricted to a single fault layer. The model can be seen as a simplified version of Morin and Acharya [3] which models quasi-static and dynamic fracture within a single planar fault layer. Specifically, we analyze and compare the layer model under different loading configurations with their analytical or experimental counterparts in the present work. The following are the novel contributions of this work.

- Crack is driven solely by the evolution of crack tip fields. Crack irreversibility is an integral feature of the model.
- The crack evolution is inherently rate–dependent and is governed by a drag parameter. Furthermore, the numerical demonstration of the influence of the drag parameter on crack evolution is provided.
- Reproduce the crack propagation under biaxial loading as demonstrated in [3] using the current finite element implementation.
- Unlike the implementation of Morin and Acharya [3] in which it is restricted to periodic boundary conditions due to the Fast Fourier Transform (FFT) based framework, the present FE implementation can model edge cracks and apply realistic boundary conditions.
- FCM model is coupled with a rate–dependent Drucker–Prager plasticity model. Basic features of metal plasticity are demonstrated.

Modeling a realistic fracture process that occurs in nature is a computationally intensive task. However, in the past few years, significant progress has been made in the computational fracture mechanics field, resulting in a much better understanding of complex fracture processes and addressing them computationally. Some of the notable fracture models are summarized in the following.

The pioneering works of Dugdale [5], and Barrenblatt [6] laid the foundation for cohesive fracture models. The central idea of cohesive zone models (CZM) is to assume an interaction force between the two crack faces. Fracture occurs when stress between the crack faces reaches a threshold strength of σ_{max}, as suggested by traction–separation law. The cohesive law presents a relation between the crack faces and the boundary tractions. The material degradation occurs due to cohesive constitutive laws, and the numerical implementation requires unique, cohesive elements in predetermined crack paths. CZMs are successful in predicting the fracture behaviour in brittle and ductile materials [7–9], interface problems [10], composite structures [11] as well.

Extended finite element method (XFEM) approach [12–14] is a class of partition of unity methods [15, 16] which enrich the finite element space with special discontinuous functions. The enrichment in XFEM happens locally near the discontinuities, which prevents the need for further re–meshing. In the XFEM model, instead of separately tracking the crack surfaces using traction separation laws, the nodes near the crack interfaces and crack tips are enriched separately with additional degrees of freedom.

Modeling cracks using finite elements requires re-meshing near the damaged region, a computationally-intensive process. It can be overcome using meshless methods [17–20] that are entirely free of underlying meshes and therefore, re-meshing is not required. Smoothed particle hydrodynamics [21, 22], element free Galerkin [17], material point methods and reproducing kernel particle method are some of the popular meshfree techniques used to model fracture. Although the meshless method seems promising to model fracture, the computational cost outweighs the finite element approach. Hence, using a coupled technique where the cracks are modeled with the meshfree method and the remaining continuum with finite element has been proposed by Rao and Rahman [23].

Recently, peridynamics models [24–27] have gained more traction in capturing the fracture phenomenon by considering the non–local effect from neighboring material points. Each material point interacts with the neighboring points within a fixed horizon in peridynamics. The interaction is based on a non–local force strain relation, which models the fracture as an emergent phenomenon. Peridynamic models are used to solve a wide range of problems in brittle [25, 28, 29] and ductile [30–32] fracture respectively.

Phase–field or diffuse fracture models proposed by [33–37] are successful in predicting the crack initiation and complex crack growth patterns through energy minimization. The scalar field or phase–field variable is controlled by the length scale parameter that controls the thickness of the crack. A variety of problems in brittle fracture [35], ductile fracture [38–40], fatigue modeling [41–43], frictional contact [44], dynamic fracture [45–47], and numerous other applications have been addressed through the utilization of phase-field driven fracture. However, the real physical meaning of the phase-field variable is still not known [48].

In the present work, a stand–alone finite element code is developed for solving linear momentum and crack field equations. The computer program is written in Fortran 90. We use MUltifrontal Massively Parallel Sparse Solver [49] (MUMPS) in the present work to solve the large linear equation system that arises from the finite element assembly. MUMPS is a Fortran based package that uses a direct method to solve the sparse system of linear equations of the form $\mathbf{Ax} = \mathbf{b}$. MUMPS utilizes a multifrontal approach to factorize the

sparse assembly system.

The manuscript is organized as follows. In Section 2 the governing equations about the complete 3D model are revisited. Additionally, the reduced form of the crack evolution equation from 3D to 1D is presented. Various components of the model, including the crack energy density functions, degradation of modulus of elasticity function, and the elastic strain energy functions under consideration, are discussed in detail. In Section 3, the numerical formulation for the 1d layer model adapted from [50] is recalled. Furthermore, the proposed staggered algorithms for brittle and ductile fracture are also discussed. Section 4 is dedicated to detailed numerical studies, starting from central cracks subjected to mode-I and mode-II loadings, edge cracks, coalescence of cracks in a single plane, and the influence of plastic strains.

2. Field crack mechanics - Layer model

This work addresses the response of fracture behavior in brittle and ductile solids by satisfying the crack evolution laws proposed in FCM. In the FCM model, the crack field $\mathbf{c}(\boldsymbol{x},t)$ and its tip field $\mathbf{t}(\boldsymbol{x},t)$ are assumed to be continuous and participate naturally in the crack evolution law by satisfying the kinematics under consideration. Under the assumption of small deformation theory, the general governing equations in 3D are

$$\begin{cases} \nabla.\boldsymbol{\sigma} = 0 & \text{balance of linear momentum (static case)} \\ \boldsymbol{\sigma} = \mathbb{C} : \boldsymbol{\varepsilon} & \text{constitutive law} \\ \boldsymbol{\varepsilon} = \frac{1}{2}(\nabla\mathbf{u} + \nabla\mathbf{u}^T) & \text{strain displacement relation} \\ \dot{\mathbf{c}} = -\text{curl}(\mathbf{c}) \times \mathbf{V} & \text{crack evolution law,} \end{cases} \tag{1}$$

where $\boldsymbol{\sigma}(\boldsymbol{x},t)$, $\boldsymbol{\varepsilon}(\boldsymbol{x},t)$ and $\mathbf{u}(\boldsymbol{x},t)$ represent the stress, strain and displacement fields that depend on damage, position and time respectively. $\mathbb{C}(|\mathbf{c}|)$ represents the fourth order elastic modulus tensor with components degraded by the amount of damage $\mathbf{c}$. $\mathbf{V}(\boldsymbol{x},t)$ represents the velocity of the crack tip field which is considered to be the driving force for the crack to evolve. Upon assuming a free energy density function [2]

$$\psi(\boldsymbol{\varepsilon}^e, \mathbf{c}, \text{curl}(\mathbf{c})) = \psi_E(\boldsymbol{\varepsilon}^e, \mathbf{c}) + \varphi(\mathbf{c}, \text{curl}(\mathbf{c})), \tag{2}$$

where ψ_E is the elastic strain energy density function that depends on strain and damage, φ is the resistance offered to the crack motion in creating new flank surfaces. $\boldsymbol{\varepsilon}^e = \boldsymbol{\varepsilon} - \boldsymbol{\varepsilon}^p$, is the elastic part of the strain tensor. $\boldsymbol{\varepsilon}$ is the symmetric part of the displacement gradient, and $\boldsymbol{\varepsilon}^p$ is the plastic strain tensor. The typical forms of ψ_E and φ are given as

$$\psi_E = \frac{1}{2}\boldsymbol{\varepsilon} : \mathbb{C}(|\mathbf{c}|)\boldsymbol{\varepsilon}, \;\; \phi = \eta(|\mathbf{c}|) + \frac{\kappa}{2}|\text{curl}(\mathbf{c})|^2, \tag{3}$$

where η is a crack energy density function that represents the energy cost for the damage to progress, and κ regularizes the crack tip field $\mathbf{t}(\boldsymbol{x},t)$. By considering the power contribution from external and internal sources, the dissipation inequality is written as

$$D = \int_{\partial V} \mathbf{t_f}.\dot{\mathbf{u}}\ da + \int_V \mathbf{b}.\dot{\mathbf{u}}\ dv - \frac{d}{dt}\int_V \psi\ dv - \frac{d}{dt}\int_V \frac{1}{2}\rho_o|\dot{\mathbf{u}}|^2\ dv, \tag{4}$$

where $\mathbf{t_f}, \mathbf{b}$ are the traction and body forces respectively. $\dot{\mathbf{u}}$ is the velocity field and ρ_o is the mass density. Substituting the free energy contribution from Eq. (2) in Eq. (4) the dissipation can be written as,

$$D = \int_V (\mathbf{T} - \partial_{\boldsymbol{\varepsilon}^e}\psi) : \mathrm{grad}(\mathbf{V})\ dv + \int_V \mathbf{T} : \dot{\boldsymbol{\varepsilon}^p}\ dv + \int_V \Big\{[-\partial_{\mathbf{c}}\psi + \mathrm{curl}(\partial_{\mathbf{t}}\psi)] \times \mathbf{t}\Big\}.\mathbf{V}\ dv + \int_{\partial v} \mathbf{V}.[(\partial_{\mathbf{t}}\psi \times \mathbf{n}) \times \mathbf{t}]\ da, \tag{5}$$

where from Eq. (5) the driving force $\mathbf{V}(\boldsymbol{x}, t)$ for the crack tip motion is deduced as

$$\mathbf{V} \rightsquigarrow \Big\{[-\partial_{\mathbf{c}}\psi + \mathrm{curl}(\partial_{\mathbf{t}}\psi)] \times \mathbf{t}\Big\}. \tag{6}$$

For completeness a more detailed derivation of Eq. (5) from Eq. (4) is shown in Appendix A.

2.1. Reduced form of the crack evolution law to 1D - A planar ansatz

Let the domain under consideration be $\Omega \in \mathbb{R}^2$, where the balance of linear momentum is satisfied and the layer L, which is embedded in Ω, where crack evolution law is to be solved. Hence, in the present work, the terms FCM model and Layer model are synonymous. The geometry with various domains under consideration for the layer model is shown in Fig. 1. The domains Ω and L are defined as

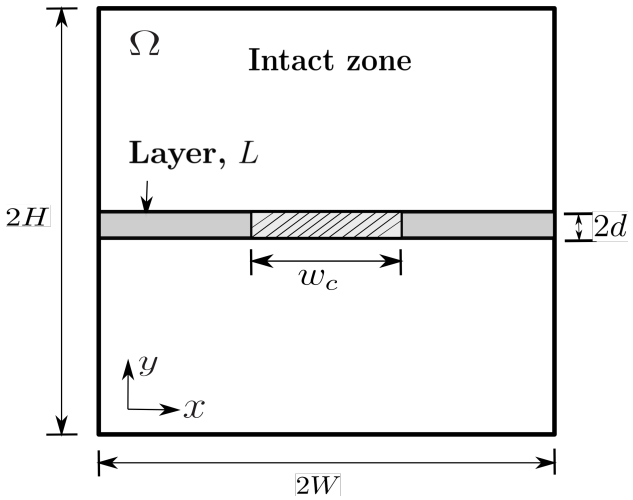

Fig. 1: Initial geometry of the layer model representing central crack (hashed portion) confined to a layer.

$$\begin{aligned}\Omega &= \{(x,y) : (x,y) \in [-W,+W] \times [-H,+H]\},\\ L &= \{(x,y) : (x,y) \in [-W,+W] \times [-d,+d]\}.\end{aligned} \tag{7}$$

In Fig. 1, 'Layer, L' indicates a singular default layer with a pre-determined crack path. The size of the domain is $2W \times 2H$. The crack field is positioned at the center of the domain, confined to the layer L with finite thickness $2d$. w_c represents the width of the crack. Assuming the vectorial crack field is confined only to the layer,

$$\mathbf{c}(\boldsymbol{x},t) = \begin{cases} w(x,t)\hat{e}_2 & \text{inside L},\\ 0 & \text{outside L}\end{cases}, \tag{8}$$

where $w(x,t)$ represents the normal component of the crack field $\mathbf{c}(\boldsymbol{x},t)$. The crack tip field and its curl are given as

$$\mathbf{t}(\boldsymbol{x},t) = -\text{curl}(\mathbf{c}) = w_{,x}\,(x,t)\hat{e}_3,\ \text{curl}(\mathbf{t}) = w_{,xx}\,(x,t)\hat{e}_2. \tag{9}$$

Assuming the velocity of the crack tip to be $\mathbf{V}(\boldsymbol{x},t) = v(x,t)\hat{e}_1$ i.e. parallel to the crack propagation direction, the crack evolution equation can be written as

$$\frac{\partial w}{\partial t} = -\frac{\partial w}{\partial x}v. \tag{10}$$

Upon substituting Eqs. (8) and (9) in Eq. (5),

$$\begin{aligned} D &= \int_V \Big\{[-\partial_{\mathbf{c}}\psi + \text{curl}(\partial_{\mathbf{t}}\psi)] \times \mathbf{t}\Big\}.\mathbf{V}\ dv\\ &= \int_L \Big\{\Big[-\frac{\partial \psi_E}{\partial c}(x,y,t) - \frac{\partial \eta}{\partial c}\,(x,t) + \text{curl}(\kappa\ \mathbf{t})\Big] \times (-w_{,x}\,\hat{e}_3)\Big\} v\hat{e}_1\ dxdy\\ &= \int_L \Big\{ -\frac{\partial \psi_E}{\partial |c|}(x,y,t)\ sgn(w(x,t)) - \frac{\partial \eta}{\partial |c|}(x,t)\ sgn(w(x,t)) + \kappa w_{,xx}\,(x,t)\Big\}(-w_{,x}\,)\ v\ dxdy, \end{aligned} \tag{11}$$

where $sgn(w) = \frac{c}{|c|}$. The layer averaged stress $G(x,t)$ is introduced as

$$G(x,t) = \frac{1}{2d}\int_{-d}^{+d} -\frac{\partial \psi_E}{\partial |c|}(x,y,t)\ sgn(w(x,t))\ dy, \tag{12}$$

and the crack energy density contributions $G_c(x,t)$ is given by

$$G_c(x,t) = \frac{\partial \eta}{\partial |c|}\ sgn(w(x,t)). \tag{13}$$

Hence, the dissipation D is given as

$$D = \int_L (-v(x,t)\ w_{,x}\,(x,t))\ [G(x,t) - G_c(x,t) + \kappa w_{,xx}\,]\ dxdy + \int_{-W}^{+W} (-v(x,t)\ \left\{ w_{,x}\,(x,t)) \int_{-d}^{+d} \left[-\frac{\partial \psi_E}{\partial |c|}(x,y,t) - G(x,t) \right] dy \right\} dx. \quad (14)$$

Due to Eq. (12), the second term in Eq. (14) becomes zero. Similar to [50], the driving force $v(x,t)$ is chosen to be

$$v(x,t) = \frac{-w_{,x}}{B_m |\mathbf{t}|^m} \left\{ G(x,t) - G_c(x,t) + \kappa w_{,xx} \right\}. \quad (15)$$

Substituting Eq. (15) in Eq. (10), the reduced form of crack evolution law in 1D is given as

$$\frac{\partial w}{\partial t} = \frac{|w_{,x}\,|^{(2-m)}}{B_m} (G(x,t) - G_c(x,t) + \kappa w_{,xx}\,), \quad (16)$$

where the parameter κ regularizes the width of the crack tip, and parameter B_m represents the drag coefficient, introducing another timescale that controls the crack velocity and bears the units as $Pa.s.m^{-1}$. G and G_c represent the driving force generated due to elastic strain energy and the energy expended to create new crack surfaces, respectively. The exponent m can take the values $0, 1, 2$ and manifest different crack evolution behavior forms. As proposed in [50], $m = 0$ gives Non–local Generalized Burger's (NGB) equation, $m = 1$ is a Non–local Level Set (NLS) and $m = 2$ gives us a Non–local Ginzburg–Landau (NGL) equations. In the present work, with $m = 1$, we studied the crack evolution equation of the NLS type.

Finally, for the layer model, the reduced form of crack evolution equation in 1D along with linear momentum balance in 2D are written as

$$\begin{cases} \nabla . \boldsymbol{\sigma} = 0 & \text{balance of linear momentum,} \\ \boldsymbol{\sigma} = \mathbb{C} : \boldsymbol{\varepsilon} & \text{constitutive law,} \\ \boldsymbol{\varepsilon} = \frac{1}{2}(\nabla \mathbf{u} + \nabla \mathbf{u}^T) & \text{strain displacement relation,} \\ \frac{\partial w}{\partial t} = \frac{|w_x|^{(2-m)}}{B_m}[G - G_c + \kappa \frac{\partial^2 w}{\partial x^2}] & \text{crack evolution law in 1D.} \end{cases} \quad (17)$$

The stress fields determined from the mechanical balance provide the driving force for the crack field. It should be noted that the crack only advances when $G >= G_c$. The objective of the present work is to solve the governing laws in Eq. (17) numerically and explore the FCM model's versatility in predicting brittle and ductile fracture.

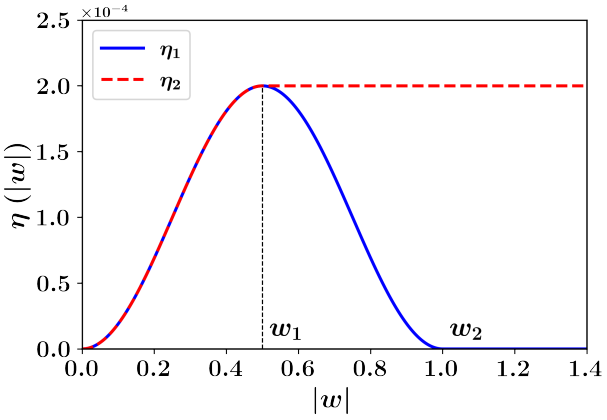

Fig. 2: Representation of various crack energy density functions as a function of damage $|w|$.

Fig. 2 shows the possible types of crack energy density functions that are chosen for the present study. The mathematical forms of η_1 and η_2 are written as

$$\eta(|w|) = \begin{cases} \eta_1(|w|) = \begin{cases} a\left[1 - \cos\left(\frac{2\pi|w|}{w_{sat}}\right)\right] & 0 \le |w| \le w_2 \\ 0 & |w| > w_2, \end{cases} \\ \\ \eta_2(|w|) = \begin{cases} \eta_1(|w|) & 0 \le |w| \le w_1 = \frac{w_2}{2} \\ \eta_1(w_1) & |w| > w_1, \end{cases} \end{cases} \tag{18}$$

where a represents the magnitude of crack energy density function, η. While the crack passes from damaged to undamaged regions, η_1 has zero energy cost, and η_2 (Griffith's type) has a finite energy cost during the damage process, which opens the possibility of crack healing. To prevent crack healing, which does not happen naturally in η_2 the crack irreversibility condition is written as

$$\frac{\partial w}{\partial t} = \begin{cases} \frac{|w_x|^{(2-m)}}{B_m}[G - G_c + \kappa\frac{\partial^2 w}{\partial x^2}] & \text{if } \left(\frac{|w_x|^{(2-m)}}{B_m}\left[G - G_c + \kappa\frac{\partial^2 w}{\partial x^2}\right]\right) > 0 \\ 0 & \text{otherwise.} \end{cases} \tag{19}$$

Detailed analysis of the nature of crack energy density functions η_1 and η_2 in dealing with crack irreversibility constraint is discussed in Section 4.4.

2.2. Models for Strain Energy functions

Various forms of strain energy functions [3, 11, 51] have been proposed in the literature to capture the fracture process under various loading scenarios. In the current FCM implementation, we mainly explore two different types of elastic strain energy density functions $(\psi_{E_{M1}}, \psi_{E_{M2}})$, which are influenced by the crack fields in different ways. In this regard, $\psi_{E_{M_1}}$ and $\psi_{E_{M_2}}$ control the crack propagation based on the crack surface normal and volumetric–deviatoric split of the strain tensor respectively.

2.2.1. Based on crack normal direction

Following Morin and Acharya [3], the elastic energy density function $\psi_{E_{M1}}$, function of strain and damage based on the crack normal direction is given as

$$\psi_{E_{M1}} = \psi_{E_{M1}}(\boldsymbol{\varepsilon}, |w|) = (1 - H(|w|))\left(\frac{1}{2}\lambda tr(\boldsymbol{\varepsilon})^2 + \mu\boldsymbol{\varepsilon} : \boldsymbol{\varepsilon}\right) + H(|w|)\left[\left(\frac{1}{2}\tilde{\lambda}tr(\boldsymbol{\varepsilon})^2 + \tilde{\mu}\boldsymbol{\varepsilon} : \boldsymbol{\varepsilon}\right) + (1 - H(\varepsilon_n))\alpha\varepsilon_n^2\right], \quad (20)$$

where ϵ_n in the last term in Eq. (20) introduces the tension compression asymmetry during fracture. Here ϵ_n and $\mathbf{n_c}$ are defined as

$$\epsilon_n = \boldsymbol{\varepsilon} : (\mathbf{n_c} \otimes \mathbf{n_c}),\ \mathbf{n_c} = \frac{\mathbf{c}}{|\mathbf{c}|}. \quad (21)$$

Based on the sign of ϵ_n, the Heaviside function $H(\varepsilon_n)$ is activated and prevents the interpenetration of crack flanks during compressive loads. Lame's constants denoted as λ and μ are involved. The degraded elastic constants $\tilde{\lambda}$ and $\tilde{\mu}$ are expressed as $f(|w|)\lambda$ and $f(|w|)\mu$ resepctively, where $f(|w|)$ signifies the degradation function responsible for reducing the material stiffness. The parameter α is defined by $\alpha = \lambda + 2\mu - [\tilde{\lambda} + 2\tilde{\mu}]$ helps to maintain the tension compression asymmetry. The stress tensor is given as

$$\boldsymbol{\sigma} = \frac{\partial\psi_{E_{M1}}}{\partial\varepsilon} = (1 - H(|w|))\left(\lambda tr(\boldsymbol{\varepsilon})\mathbf{I} + 2\mu\boldsymbol{\varepsilon}\right) + H(|w|)\left[\left(\tilde{\lambda}tr(\boldsymbol{\varepsilon})\mathbf{I} + 2\tilde{\mu}\boldsymbol{\varepsilon}\right) + (1 - H(\varepsilon_n))\alpha\varepsilon_n\mathbf{n_c} \otimes \mathbf{n_c}\right]. \quad (22)$$

The fourth order stiffness tensor is defined as

$$\mathbb{C} = (1 - H(|w|))\left(\lambda\mathbf{I} \otimes \mathbf{I} + 2\mu\mathbb{I}\right) + H(|w|)\left[\left(\tilde{\lambda}\mathbf{I} \otimes \mathbf{I} + 2\tilde{\mu}\mathbb{I}\right) + (1 - H(\varepsilon_n))[\alpha\mathbf{n_c} \otimes \mathbf{n_c} \otimes \mathbf{n_c} \otimes \mathbf{n_c}]\right]. \quad (23)$$

2.2.2. Based on volumetric–deviatoric split

The elastic strain energy density function based on the volumetric–deviatoric split is given as

$$\psi_{E_{M2}} = \psi_{E_{M2}}(tr(\boldsymbol{\varepsilon}), |w|) = (1 - H(|w|))\left(\frac{1}{2}Ktr(\boldsymbol{\varepsilon}^2) + \mu\boldsymbol{\varepsilon}^{'} : \boldsymbol{\varepsilon}^{'}\right) + H(|w|)\left[H(tr(\boldsymbol{\varepsilon}))\left(\frac{1}{2}\tilde{K}tr(\boldsymbol{\varepsilon}^2) + \tilde{\mu}\boldsymbol{\varepsilon}^{'} : \boldsymbol{\varepsilon}^{'}\right) + (1 - H(tr(\boldsymbol{\varepsilon})))\left(\frac{1}{2}Ktr(\boldsymbol{\varepsilon}^2) + \tilde{\mu}\boldsymbol{\varepsilon}^{'} : \boldsymbol{\varepsilon}^{'}\right)\right], \quad (24)$$

where $tr(\varepsilon)$ denotes the trace of strain tensor, and K and μ represent the undamaged bulk and shear modulus respectively. The damaged bulk and shear moduli $\tilde{K}(|w|)$ and $\tilde{\mu}(|w|)$ are expressed as $f(|w|)K$ and $f(|w|)\mu$. $\boldsymbol{\varepsilon}^{'}$ represents the deviatoric strain tensor. Unlike $\psi_{E_{M1}}$ which is a function of normal strain to the crack surface, the distinction between tension and compression fracture in $\psi_{E_{M2}}$ is influenced by volumetric strains. The stress tensor $\boldsymbol{\sigma}$ is given as

$$\begin{aligned}\boldsymbol{\sigma} = (1 - H(|w|))\Big(Ktr(\boldsymbol{\varepsilon})\mathbf{I} + 2\mu\boldsymbol{\varepsilon}^{'}\Big) + \\ H(|w|)\Big[H(tr(\boldsymbol{\varepsilon}))\Big(\tilde{K}tr(\boldsymbol{\varepsilon})\mathbf{I} + 2\tilde{\mu}\boldsymbol{\varepsilon}^{'}\Big) + (1 - H(tr(\boldsymbol{\varepsilon})))\Big(Ktr(\boldsymbol{\varepsilon})\mathbf{I} + 2\tilde{\mu}\boldsymbol{\varepsilon}^{'}\Big)\Big]. \quad (25)\end{aligned}$$

The fourth order stiffness tensor for $\psi_{E_{M2}}$ is

$$\begin{aligned}\mathbb{C} = (1 - H(|w|))\Big(K\mathbf{I}\otimes\mathbf{I} + 2\mu\Big(\mathbb{I} - \frac{\mathbf{I}}{3}\Big)\Big) + \\ H(|w|)\Big[H(\varepsilon_{kk})\Big(\tilde{K}\mathbf{I}\otimes\mathbf{I} + 2\tilde{\mu}\Big(\mathbb{I} - \frac{\mathbf{I}}{3}\Big)\Big) + (1 - H(\varepsilon_{kk}))\Big(K\mathbf{I}\otimes\mathbf{I} + 2\tilde{\mu}\Big(\mathbb{I} - \frac{\mathbf{I}}{3}\Big)\Big)\Big]. \quad (26)\end{aligned}$$

The Heaviside function which acts as a controlling parameter to differentiate the damaged and intact zones is defined as

$$H(x) = \begin{cases} 1 & \text{if } x > 0 \\ 0 & \text{if } x \leq 0. \end{cases} \quad (27)$$

The quadratic degradation function $f(|w|)$ as a function of damage w is given as

$$f(|w|) = \begin{cases} 1 - \frac{2(1-f_m)}{\bar{w}}|w| + \frac{(1-f_m)}{\bar{w}^2}|w|^2 & 0 \leq |w| \leq \bar{w} \\ f_m & |w| > \bar{w}, \end{cases} \quad (28)$$

where $\bar{w}$ represents the threshold of the damage w, and f_m is the minimum value of elastic modulus degradation. Before proceeding to the numerical schemes adopted for the present study, we first chose to non–dimensionalize the system of governing equations in Eq. (17). By assuming length (l), which can be domain width or height, load rate (l_r) and shear modulus (μ) as the primary variables, the non–dimensional parameters are given as

$$\tilde{\sigma} = \frac{\sigma}{\mu}, \tilde{x} = \frac{x}{l}, \tilde{t} = l_r t, \tilde{w}_c = \frac{w_c}{l}, \tilde{h}_c = \frac{h_c}{l}, \tilde{\lambda} = \frac{\lambda}{\mu}, \tilde{a} = \frac{a}{\mu}, \tilde{k} = \frac{k}{\mu l^2}, \tilde{B}_m = \frac{lB_m l_r}{\mu}, \quad (29)$$

The quasi static non–dimensional system is given as

$$\begin{cases} \tilde{\nabla}.\tilde{\boldsymbol{\sigma}} = 0 & \text{balance of linear momentum,} \\ \tilde{\boldsymbol{\sigma}} = \tilde{\mathbb{C}} : \boldsymbol{\varepsilon} & \text{constitutive law,} \\ \boldsymbol{\varepsilon} = \frac{1}{2}(\tilde{\nabla}\tilde{\mathbf{u}} + \tilde{\nabla}\tilde{\mathbf{u}}^T) & \text{strain displacement relation,} \\ \frac{\partial w}{\partial \tilde{t}} = \frac{|w_{\tilde{x}}|^{(2-m)}}{\tilde{B}_m}[\tilde{G} - \tilde{G}_c + \tilde{\kappa}\frac{\partial^2 w}{\partial \tilde{x}^2}] & \text{crack evolution law in 1D.} \end{cases} \tag{30}$$

From hereon all the $\tilde{}$ exponents are dropped and all the parameters are non–dimensional unless explicitly stated.

3. Numerical scheme

To address the system of equations shown in Eq. (30), two distinct solvers are employed for linear momentum and crack evolution equations. The balance of linear momentum is tackled using the standard Galerkin finite element approach, while a finite difference approach, incorporating the upwinding technique [52], is utilized for the time-dependent crack evolution. The governing equations are solved in a staggered manner as described in Section 3.1.

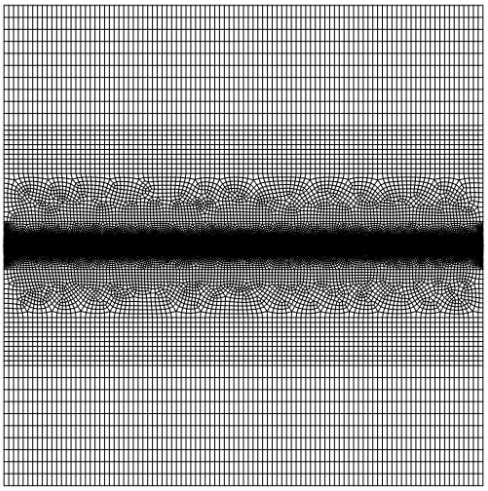

Fig. 3: Geometry with refined mesh inside the layer.

The finite element domain discretization is shown in Fig. 3. The mesh is highly refined inside the layer to accurately capture the stress singularities in the crack region and gradually transitions to a coarser mesh near the boundary. The mesh inside the layer is completely structured, incorporating a finite-difference grid. It employs quadrilateral elements with full integration, totaling approximately 40,000 elements.

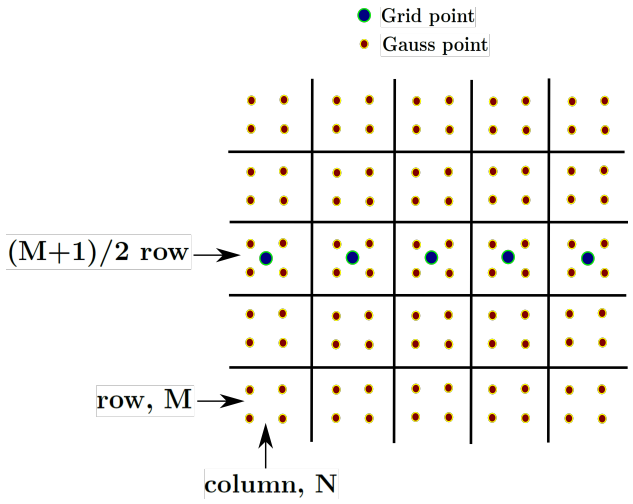

Fig. 4: Schematic showing FD grid embedded in the finite element mesh inside the layer.

As mentioned in [50], the layer stress G in Eq. (12) corresponding to finite difference grid is calculated as follows. The finite element mesh inside the layer and the insertion of the finite difference grid are shown in Fig. 4. It is also shown that each element in the finite element mesh contains four Gauss points, and each column is assigned to a finite difference grid point. The number of rows of elements and columns in the layer are M and N respectively. Then the center of each column in the (M+1)/2 row inside the layer corresponds to a grid point in the finite difference grid. Let $\psi_{E,w}(l,k)$ denote the value of integrand in Eq. (12) at grid point k and Gauss point l respectively. Then the value of G at grid point x_k is calculated as

$$G(x_k) = \frac{1}{N_l}\sum_{k=1}^{N_l}\psi_{E,w}(l,k), \tag{31}$$

where N_l denotes the number of Gauss points in column N.

3.1. Algorithm for crack evolution

For the sake of completeness, the crack evolution algorithm which incorporates the up-winding feature initially proposed by [52] and subsequently modified by [50] is presented in the current section. It is worth emphasizing that the crack evolution equation, sub–equation 4 of Eq. (17) bears a resemblance to the evolution of the plastic distortion tensor outlined in [50, 52]. As elucidated in [50], the fundamental concept behind the linearization of crack evolution algorithm involves deducing the direction of wave propagation and incorporating it into the actual non-linear crack evolution equation. In this regard, we consider the first variation of the sub–equation 4 of Eq. (17), and the initial term in Eq. (32) signifies the linearized wave-like behavior, a concept also discussed in references [50, 52]. Assuming Δh and Δt represent the spatial and temporal increments respectively, the linearization of the crack evolution equation given in Eq. $(17)_4$ is as follows

$$\delta w_t^k(x_h) = -(2-m)\left[\frac{-sgn(w_x^k(x_h))}{B_m}\right]|w_x^k(x_h)|^{1-m}\left[G^k(x_h) - G_c^k(x_h) + \kappa w_{xx}^{k+1}(x_h)\right] + \frac{|w_x^k(x_h)|^{2-m}}{B_m}\left[\kappa\delta w_{xx}^k(x_h)\right] + \frac{|w_x^k(x_h)|^{2-m}}{B_m}\left[G_c^{'}(x_h)\delta w^k(x_h)\right], \quad (32)$$

where $w^k(x_h)$ represents the value of damage at k^{th} time step and h^{th} grid point respectively. The velocity of the crack tip at grid point x_h and time step k is given as

$$C^k(x_h) = (2-m)\left[\frac{-sgn(w_x^k(x_h))}{\tilde{B}_m}\right]|w_x^k(x_h)|\left[G^k(x_h) - G_c^k(x_h) + kw_{xx}^{k+1}\right]. \quad (33)$$

By using central difference to approximate the first and second order derivatives of the crack field are given as,

$$w_x^k(x_h) = \frac{w^k(x_{h+1}) - w^k(x_{h-1})}{2\Delta h}, \quad (34)$$

$$w_{xx}^k(x_h) = \frac{w^k(x_{h+1}) + w^k(x_{h-1}) - 2w^k(x_h)}{\Delta h^2}. \quad (35)$$

Depending on the sign of velocity $C^k(x_h)$ the upwinding is calculated as

$$w_x^k = \begin{cases} \frac{1}{\Delta h}(w^k(x_{h+1}) - w^k(x_h)) & \text{if } C^k(x_h) < 0 \\ \frac{1}{\Delta h}(w^k(x_h) - w^k(x_{h-1})) & \text{if } C^k(x_h) > 0 \\ \frac{1}{2\Delta h}(w^k(x_{h+1}) - w^k(x_{h-1})) & \text{if } C^k(x_h) = 0. \end{cases} \quad (36)$$

To ensure the stability of the solution, the chosen timestep for a particular iteration must adhere to the CFL conditions. The calculation of the timestep is as follows

$$\Delta t^k = min\left[\frac{\Delta h}{C(x_k)}, \frac{\tilde{B}_m}{|\phi_x(x_k)|^{2-m}(-G_c(x_k))'}\right]. \quad (37)$$

The crack field is updated as

$$w^{k+1}(x_h) - \kappa\Delta t^k \frac{|w^k(x_h)|^{2-m}}{B_m} w_{xx}^{k+1}(x_h) = w^k(x_h) + \Delta t^k \frac{|w^k(x_h)|^{2-m}}{B_m}\left[G^k(x_h) - G_c^k(x_h)\right]. \quad (38)$$

Eq. (38) yields a linear system of equations for all the finite difference grid points where w^{k+1} is calculated. The proposed staggered scheme for brittle fracture problem is shown in Algorithm 1.

Algorithm 1: Staggered algorithm for brittle fracture using FCM from $t_n \rightarrow t_{n+1}$

Input: Initialize the primary variables displacement $u = u_n$ and crack field $w = w_n$

. /* The initial crack field at t_o is the equilibrated field. */

while $n = 1 : nsteps$ **do**

  /* Loop over load steps */

  Update the prescribed loading at t_{n+1}. Solve for u_{n+1} by keeping crack field w_n frozen.

  /* Solve mechanical balance using standard Galerkin Finite Element appraoch. */

  while $|\mathrm{R}| < tol$ **do**

    /* Iterate over Newton--Raphson loop until residue is below tolerance. */

    Calculate material property matrix $\mathbb{C}(\varepsilon)$ from Eq. (23) or Eq. (26).

    Calculate tangent stiffness $K_T = \int B^T \mathbb{C}(\varepsilon) B$.

    Calculate Residue $R = F_{int} - F_{ext}$.

    Solve δu using $K_T \delta u = -R$.

    $u_{n+1} \leftarrow u_n + \delta u$.

  Update elastic strain energy G and crack energy density G_c contributions inside the layer.

  /* Solve crack evolution equation using finite difference upwind scheme */

  By keeping displacement u_{n+1} frozen find w_{n+1} using the linearly implicit scheme as shown in Section 3.1.

  Update the time step and repeat the above procedure

3.2. A rate–dependent Drucker–Prager plasticity for ductile fracture

To predict the ductile fracture due to permanent deformation or plastic strains, a rate–dependent power law based model is utilized as detailed in the present section. In the context of non–associated flow rule, the plastic potential and yield functions are considered to be separate. However, in rate–dependent plasticity, the plastic strain rate is given as

$$\dot{\boldsymbol{\varepsilon}}^p = \vartheta \frac{\partial g}{\partial \boldsymbol{\sigma}}, \tag{39}$$

where ϑ is the plastic multiplier and $g(\sigma)$ is the plastic potential function. The plastic potential is defined as

$$g = \tau - \alpha_\psi p, \tag{40}$$

where α_ψ is the tangent of the dilatation angle. p and τ are the pressure and effective deviatoric stress, respectively, and are defined as

$$p = \frac{-\boldsymbol{\sigma}_{kk}}{3}; \tau = \sqrt{\frac{\boldsymbol{\sigma}' : \boldsymbol{\sigma}'}{2}}, \tag{41}$$

where $\boldsymbol{\sigma}_{kk}$ and $\boldsymbol{\sigma}'$ represent the trace and deviatoric part of stress tensor respectively. The yield function Y is given as

$$Y = \tau - \alpha p - K(e^p),\ \alpha = \tan(\beta), \tag{42}$$

where α and e^p are the tangent of the friction angle (β) and effective plastic strain respectively. The linear isotropic hardening function $K(e^p)$ is given as

$$K(e^p) = \sigma_{yo} + \mathcal{H}e^p, \tag{43}$$

where σ_{yo} is the yield stress and $\mathcal{H}$ is the hardening constant. The perfect plasticity is obtained by setting $\mathcal{H} = 0$. The plastic multiplier and normal to the plastic potential are given as

$$\vartheta = \frac{\dot{e}^p}{\eta_g}, \qquad \frac{\partial g}{\partial \boldsymbol{\sigma}} = \frac{\alpha_\psi}{m}\mathbb{I} + \frac{\boldsymbol{\sigma}'}{2\tau}, \qquad \eta_g = \left\| \frac{\partial g}{\partial \boldsymbol{\sigma}} \right\|, \tag{44}$$

where η_g is the magnitude of $\frac{\partial g}{\partial \boldsymbol{\sigma}}$. By substituting Eq. (44) in Eq. (39), the plastic strain rate is given as

$$\dot{\boldsymbol{\varepsilon}}^p = \frac{\left(\frac{\|\tau - \alpha p\|}{K(e^p)}\right)^{\frac{1}{m}}}{\eta_g} \frac{\partial g}{\partial \boldsymbol{\sigma}}. \tag{45}$$

The staggered rate–dependent plasticity algorithm chosen for ductile fracture is shown in Algorithm 2. To make the implementation simpler, plastic strains are updated explicitly. Therefore, the material property matrix and the stress tensors remain the same as in a brittle fracture. However, the only difference is that all the concerned quantities are evaluated based on elastic strains instead of total strains. The time step calculation in the ductile case is given as

$$\Delta t = min\left[\frac{\Delta h}{max(C(x_k))}, \frac{\tilde{B}_m}{max(|\phi_x(x_k)|^{2-m}(-G_c(x_k)'))}, dt_f\left(\frac{0.002}{max(\dot{e}^p)}\right)\right], \tag{46}$$

where dt_f is a factor ranging from $0.1 - 1.0$ is chosen for the stability of the solution.

Algorithm 2: Staggered algorithm for ductile fracture using FCM from $t_n \rightarrow t_{n+1}$.

Input: Initialize the primary variables displacement $u = u_n$, crack field $w = w_n$ and plastic strain tensor $\varepsilon^p = \varepsilon^p_n$

. /* The initial crack field at t_o is the equilibrated field */

while $n = 1 : nsteps$ **do**

  /* Loop over load steps */

  Update the prescribed loading at t_{n+1}. Solve for u_{n+1} by keeping crack field w_n frozen.

  /* Solve Mechanical balance using standard Galerkin Finite Element approach. */

  while |R|<tol **do**

    /* Iterate over Newton Raphson loop until residue is below tolerance. */

    Calculate material property matrix $\mathbb{C}(\varepsilon^e)$ from Eq. (23) or Eq. (26) using elastic strain tensor, $\varepsilon^e = \varepsilon - \varepsilon^p$.

    Calculate tangent stiffness $K_T = \int B^T \mathbb{C}(\varepsilon^e) B$.

    Calculate Residue $R = F_{int} - F_{ext}$.

    Solve δu using $K_T \delta u = -R$.

    $u_{n+1} \leftarrow u_n + \delta u$.

  Update plastic strain tensor as $\varepsilon^p_{n+1} = \varepsilon^p_n + \Delta t \dot{\varepsilon}^p$.

  Update elastic strain energy G and crack energy density G_c contributions inside the layer.

  /* Solve crack evolution equation using finite difference upwind scheme */

  By keeping displacement u_{n+1} frozen find w_{n+1} using the linearly implicit scheme as shown in Section 3.1.

  Update the timestep and repeat the above procedure.

4. Numerical studies

In the present section, we demonstrate a few benchmark cases based on the FCM model using the numerical implementation as shown in Section 3. Noteworthy is that many of these case studies are motivated by the work of [3]. The initial geometry setup under consideration is shown already in the Fig. 1. The domain contains a central crack of width $w_c = 0.3$ and thickness $2d = 0.002$ positioned inside the layer. The near tip analytical solution for normal stress given by Westergaard [53] for an infinite plate with a central crack of width $2w_c$ subjected to a remote mode-I loading of σ_∞ is given as

$$\sigma_{22} = \frac{\sigma_\infty}{\sqrt{1 - (\frac{w_c}{x})^2}}. \tag{47}$$

First, the static crack tip stresses are compared for mode-I and mode-II loading against their analytical counterparts. Fig. 5 shows the comparison of averaged normalized $\sigma_{22}/\sigma_\infty$ stress for mode-I and $\sigma_{12}/\sigma_\infty$ for mode-II inside the layer. A good match is observed for both the elastic strain energy functions $(\psi_{E_{M_1}}, \psi_{E_{M_2}})$ under consideration. It is evident that the

stresses away from the crack tip reach σ_∞. From Fig. 5 it is evident that the FCM model can capture the inverse square root singularities near the crack tip precisely. Additionally, it is important to note that stresses within crack regions are not entirely zero; instead, they are influenced by the f_m value as defined in Eq. (28). For the sake of numerical convenience, the f_m has been set to 0.001 in the current study.

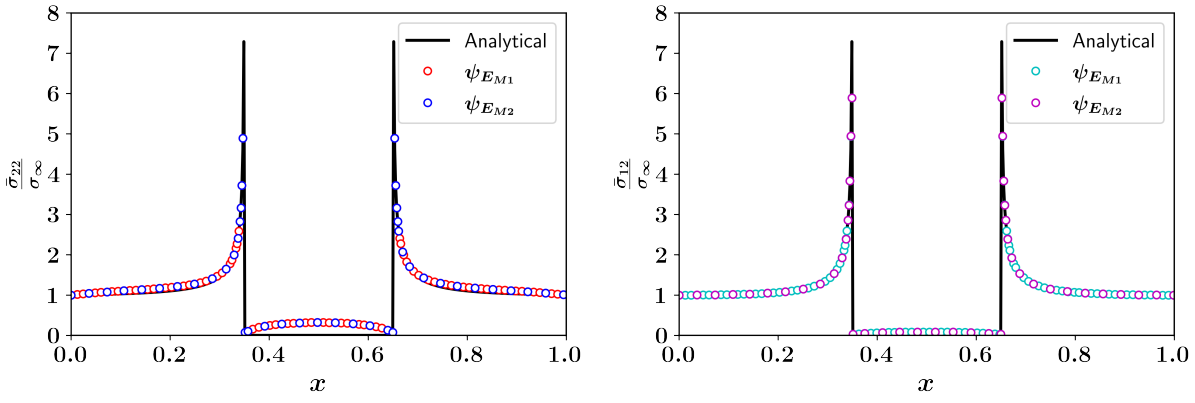

(a) (b)

Fig. 5: Comparison of normalized analytical and numerical stresses for different strain energy models under (a) Mode-I and (b) Mode-II loading conditions.

4.1. Initial crack equilibrium

For the initial crack field under consideration, even in the absence of external loading, i.e., $G = 0$, some equilibrium may exist due to the interplay between the crack–tip energy density (Laplacian term) and crack energy density contribution. Here, the equilibrium is investigated for the crack energy density function η_2 with zero surface energy cost. Defining $\varrho = \kappa/a$ as the ratio of crack–tip energy density and the magnitude of crack energy density term. Different values of ϱ are investigated over a range of $[0, 0.1, 1000]$. With no external energy supplied and $\varrho = 0$ or when the crack–tip energy density is null, any chosen crack field is already in equilibrium, and no motion in the crack is observed. Fig. 6 shows the effect of ϱ for 0.1 and 1000 respectively. In Fig. 6a it can be noted that there is no noticeable change from the initial to the equilibrated positions. The crack energy density term tries to balance with the crack–tip energy density and acquires a stable position of the crack field. However, as shown in Fig. 6b for $\varrho = 1000$, no stable equilibrium for the crack field is found because the crack–tip energy density dominates the crack energy density making the initial crack field diffuse over the layer completely. So, this high ϱ value choice makes it unsuitable to maintain the sharp crack fronts. In the forthcoming sections, for all the case studies under consideration, unless explicitly stated to maintain sharp crack fronts, $\varrho = 0.1$ is maintained.

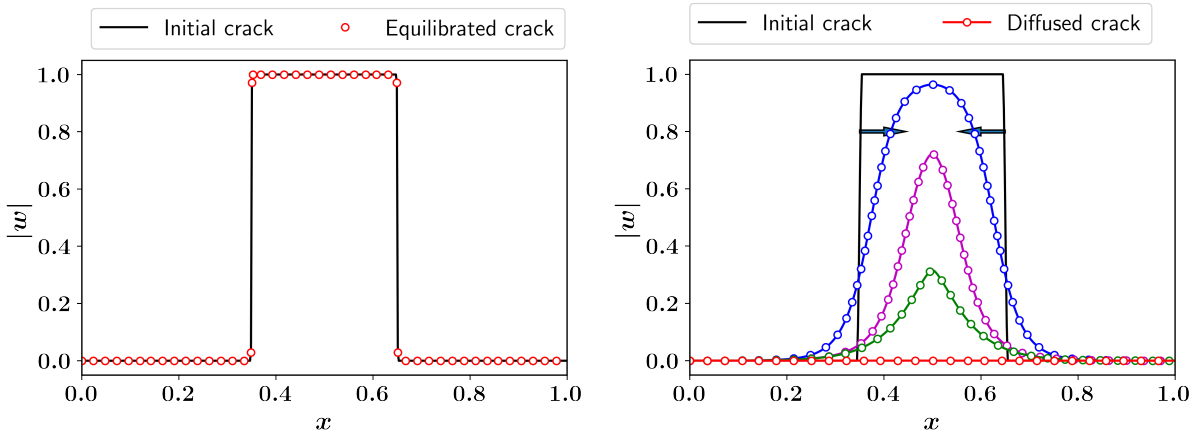

(a) (b)

Fig. 6: Effect of ρ, the ratio of crack–tip energy density and the magnitude of crack energy density function on the crack equilibria corresponding to (a) $\varrho = 0.1$, (b) $\varrho = 1000$. The inward arrays shows the direction diffused crack.

4.2. Brittle fracture

In this section, using the layer model in FCM, we present several paradigmatic examples related to brittle fracture. For all the case studies under consideration, an equilibrated crack field with sharp crack fronts is assumed as the initial condition prior to loading.

4.2.1. Central crack subjected to Mode-I loading

Here, the response of crack evolution under pure mode-I loading is presented. Since the simulations are quasi–static, a small drag parameter B_m, is chosen for a constant loading rate l_r. The sensitivity study on the stress–strain curves for different B_m values is shown in Fig. 7. As the drag parameter B_m decreases, the crack finds enough time to progress, which triggers the early softening response or the loading behavior becomes rate–independent. However, as shown in Eq. (37) reducing B_m also impacts the time step, which in turn increases the computational cost. Therefore, in the present work, a convenient value of $B_m = 0.01$ is chosen for all the simulations unless explicitly stated.

It should be noted that the same (see Fig. 7) rate–independent behavior can also be achieved by reducing the load rate at a constant B_m. Different parameters chosen for the present numerical simulations are shown in Table 1. Before loading the specimen, an initial equilibrated crack field is attained by maintaining the ratio between the crack–tip energy density and magnitude of crack energy density term to 0.1. The small ratio of ϱ also helps to keep the crack fronts sharp instead of diffusing, as shown in Fig. 6b. To achieve a better numerical convergence by avoiding a sharp contrast modulus between the intact and the damaged regions, the degradation parameter f_m is chosen to be 0.001 and not null. The ratio between Lame's parameters (λ/μ) is chosen to be 2.

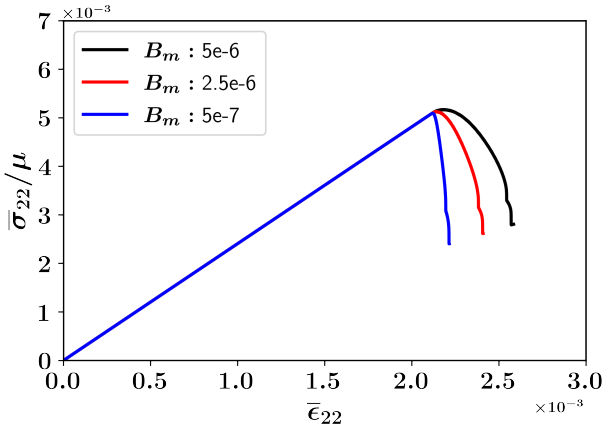

Fig. 7: Sensitivity study of drag parameter B_m on stress strain behaviour.

Table 1: Non–dimensional parameters for Mode-I loading.

Crack evolution	B_m	5e-7
	κ	1e-5
	m	1.0
	l_r	1.0
	$2d$	0.002
Degradation function	f_m	0.001
	$\bar{w}$	1.0
Crack energy density function	a	1e-4
	w_{sat}	1.0

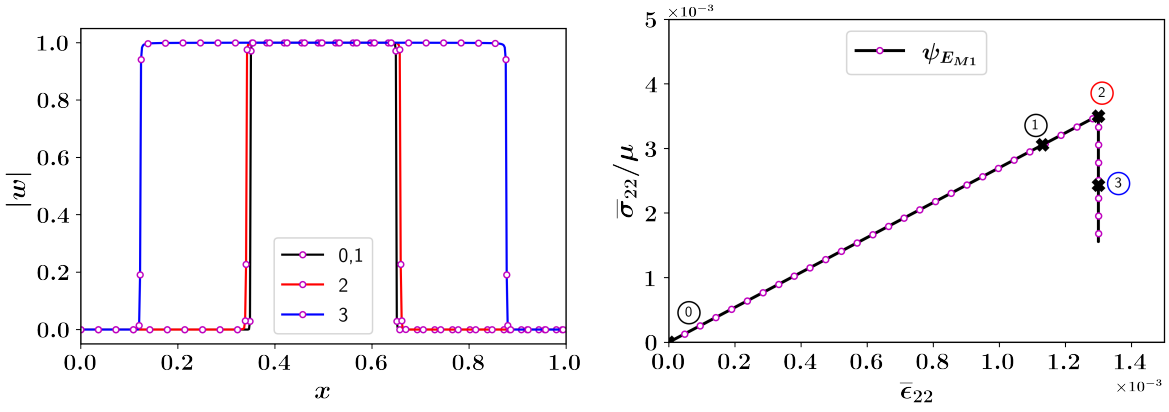

(a) (b)

Fig. 8: Crack propagation (a) and associated softening in stress–strain curve (b) representing different phases of propagation for the elastic strain energy function, $\psi_{E_{M1}}$ under mode-I loading.

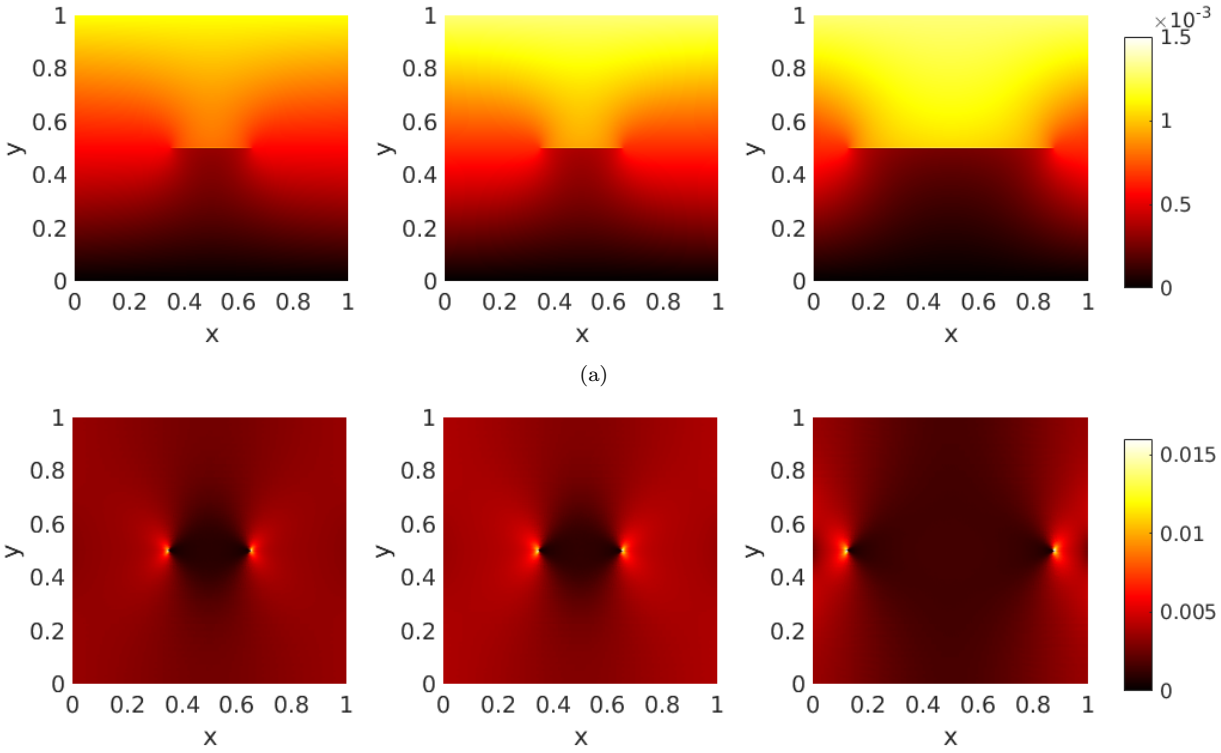

(a)

(b)

Fig. 9: Distribution of displacement u_2 (a) and stress fields σ_{22} (b) in y-direction, under mode-I loading for $\psi_{E_{M1}}$ following different stages of crack propagation in Fig. 8b from left to right.

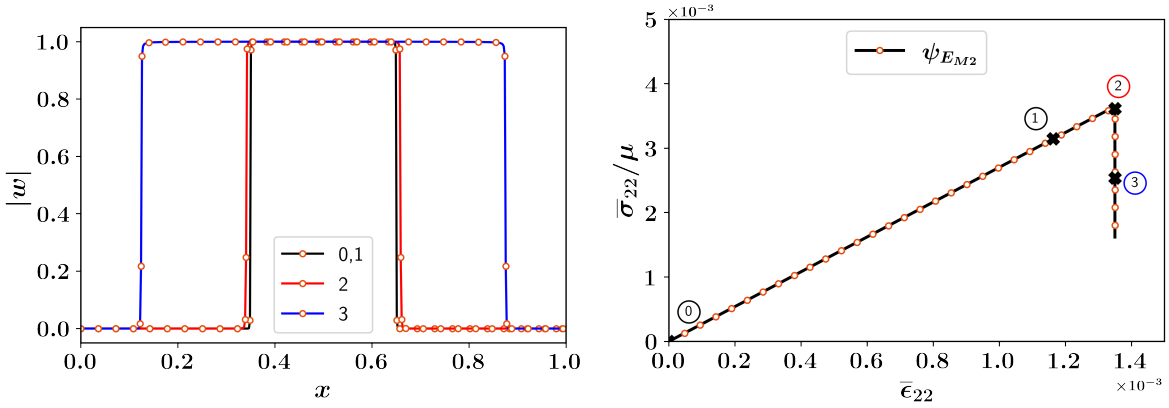

(a)

(b)

Fig. 10: Crack propagation (a) and associated softening in stress–strain curve (b) representing different phases of propagation for the elastic strain energy function, $\psi_{E_{M2}}$ under mode-I loading.

The evolution of crack field and its influence on stress–strain curves for the strain energy functions under consideration are shown in Figs. 8 and 10 respectively. Different phases in crack evolution under mode-I loadings are as follows

- A linear evolution accompanies the first phase in stress strain curve ⓪ – ① where no physical movement of the crack is visible. In this regime, the strain energy release rate is less than the crack energy density contribution, i.e., $G < G_c$, which results in no net driving force for the crack to move.

- A stable crack movement is followed with a linear regime from ① – ② that corresponds to $G = G_c$ where strain energy release rate balances the crack energy density rate, resulting in stable crack propagation. However, in this regime, crack propagation is possible only with an increase in loading.

- Beyond the position ②, the crack movement happens without any increase in the external load. It results in a softening phase where the crack moves entirely inside the layer, breaking the specimen into two halves. Position ② also suggests threshold stress, which is similar to Peierls stress for dislocations. It is also worth mentioning that the present crack evolution model is similar to the continuum dislocation theory of Zhang [50]. The third phase corresponds to a softening regime from ② – ③.

- It is to be noted that both the strain energy models can predict the mode-I crack behavior as suggested by the classical fracture mechanics.

- The displacement and stress contours for mode-I loadings are shown in Figs. 9a and 9b. The stress concentration near the cracktips is clearly visible in Fig. 9b. It is also worth mentioning that as the crack propagates, there is an elevation in concentration of σ_{22} component near crack tips which might accelerate the crack.

4.2.2. Influence of the magnitude of crack energy density function

The study on mode-I crack propagation presented in Section 4.2.1 highlights the fact that if the energy release rate is more than the magnitude of the crack energy density function, it imparts a net driving force for the crack motion. Therefore, the onset of crack propagation is dictated by the crack energy density function magnitude. Further analysis was performed for $a/\mu = 10^{-6}, 10^{-5}, 10^{-4}$. Fig. 11a shows the sensitivity on stress–strain curves for mode-I loading. The FCM model captures all the crack propagation phases i.e. linear regime, stable and unstable phases, respectively. Larger a/μ magnitude delays the crack motion, indicating that more energy needs to be supplied for the crack with higher crack energy density. Fig. 11b shows that the non–dimensional term $max(\bar{\sigma}_{22}/\mu)/\sqrt{a/\mu}$ is scaled to be a constant value or insensitive to a/μ.

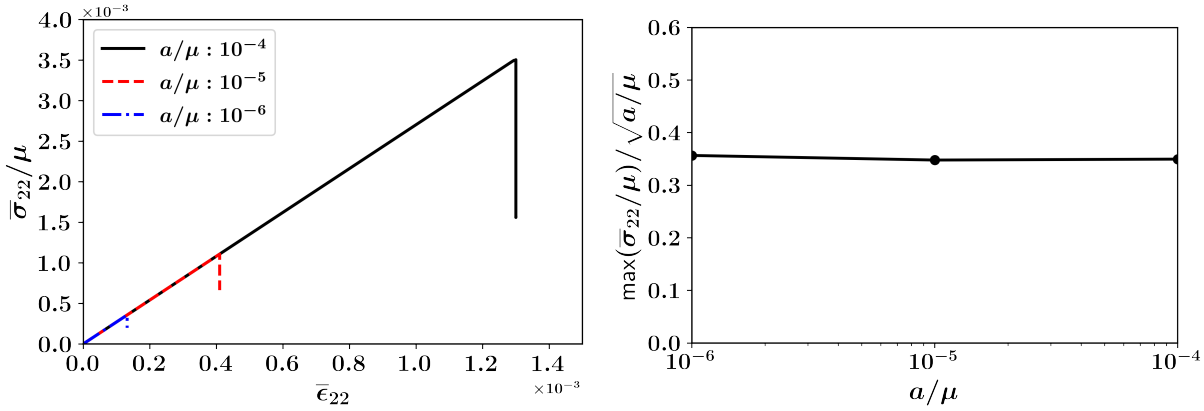

(a) (b)

Fig. 11: Influence of a/μ (non–dimensional crack energy density) ratio on (a) stress strain curves, (b) scaling of non–dimensional peak stress with a/μ.

4.2.3. Strength and toughness predictions of FCM model

Further, predicted critical strength σ_c and fracture toughness K_{Ic} by the FCM model are analyzed for the crack energy density functions η_1 and η_2 subjected to mode-I tensile loading. The study is about obtaining the threshold normal stress values for the crack widths ranging from 0.2–0.4. The macroscopic tensile stress, $\bar{\sigma}_{22}/\mu$ and crack tip stresses at the onset of crack propagation are shown in Fig. 12a and Fig. 12b respectively. It is observed that the macroscopic stress increases with the diminution of crack width w_c/l. It indicates that cracks with smaller widths require more energy to evolve. From Fig. 12b, it is also evident that crack tip stresses scale to some constant value up to the crack width of 0.4, beyond which the crack tip stresses exhibit a different scaling. It shows the prediction of critical stress σ_c to some constant value indicating some local stress criterion by the FCM model. The probable reason for the different scaling behavior of crack tip stresses might be the effect of thickness, which is not considered in the present study. The mode-I stress intensity factor for a central crack of width $2w_c$ is given as

$$K_I = \bar{\sigma}_{22}\sqrt{\pi w_c}. \tag{48}$$

Fig. 13 shows the variation of non–dimensional stress concentration factor $K_I/(\mu\sqrt{\kappa/a})$ vs. the crack width w_c/l. It is worth mentioning that the stress intensity factor is scaled to a constant value, that represents the prediction of apparent fracture toughness K_{Ic} of the material. The predictions made by the FCM model agree with [54] where both strength and fracture toughness criteria must simultaneously be fulfilled for the crack to grow. It is also worth mentioning that both the crack energy density functions under consideration in the FCM model made similar predictions on σ_c and, K_{Ic} respectively.

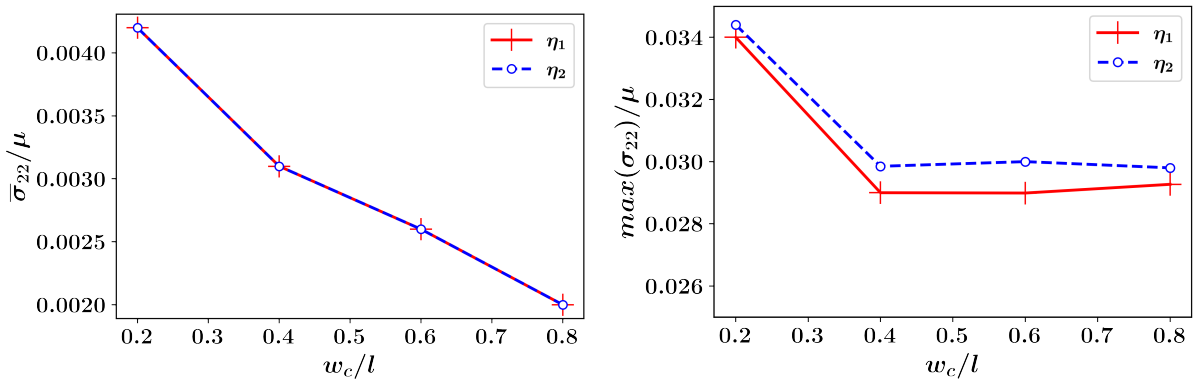

(a) (b)

Fig. 12: Influence of w_c/l (non–dimensional crack width) on average macroscopic stress (a) and corresponding cracktip stress (b) for the crack energy functions η_1 and η_2.

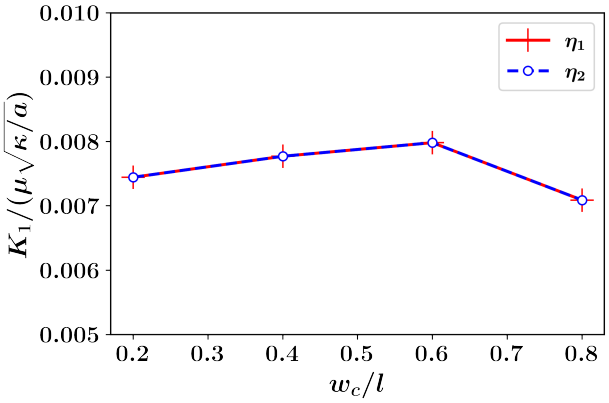

Fig. 13: Predictions of stress intensity factor K_I for mode-I loading using FCM model.

4.2.4. Mode-II Loading

The response of the FCM model under the shear test or mode-II loading is discussed in this section. The same square domain as shown in Fig. 1 with central crack of width $w_c = 0.3$ is considered, and a shear strain ε_{12} is applied on the top surface. The boundary conditions are applied such that the vertical surfaces are maintained parallel to each other by restricting the y-direction displacement to zero. The drag parameter, B_m value of 5e-7 is maintained to precisely capture the onset of unstable crack propagation. For the strain energy functions under consideration Figs. 14 and 15 shows different phases of crack propagation along with their stress-strain curves. It is worth mentioning that the FCM model can capture all the phases of crack propagation from a linear regime ⓪–①, stable phase ①–② and unstable region ②–③. In Fig. 16a it is observed that due to cracking, the top portion of the domain slides for the bottom portion near the crack surface. The stress concentration near crack tips is growing in Fig. 16b which indicates the acceleration of the crack as it evolves.

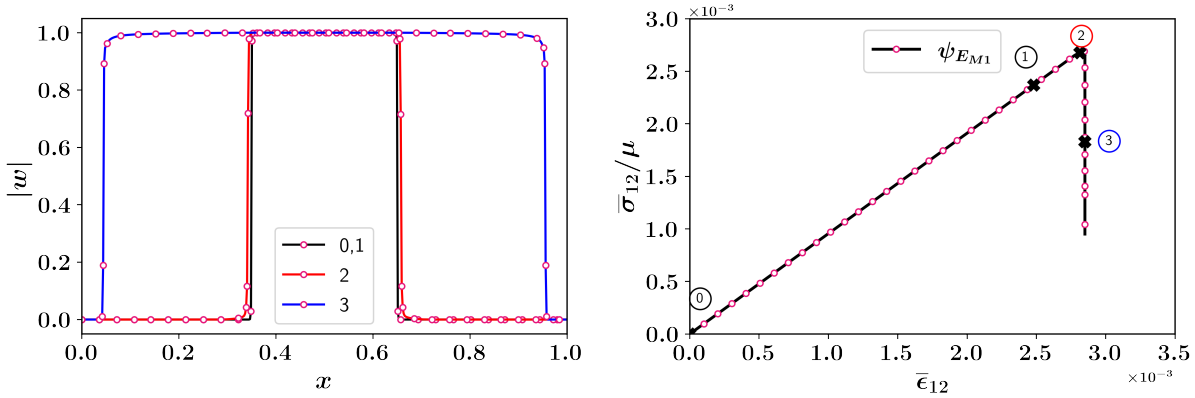

(a) (b)

Fig. 14: Crack propagation (a) and associated softening in stress-strain curve (b) representing different phases of propagation for the elastic strain energy function, $\psi_{E_{M1}}$ under mode-II loading.

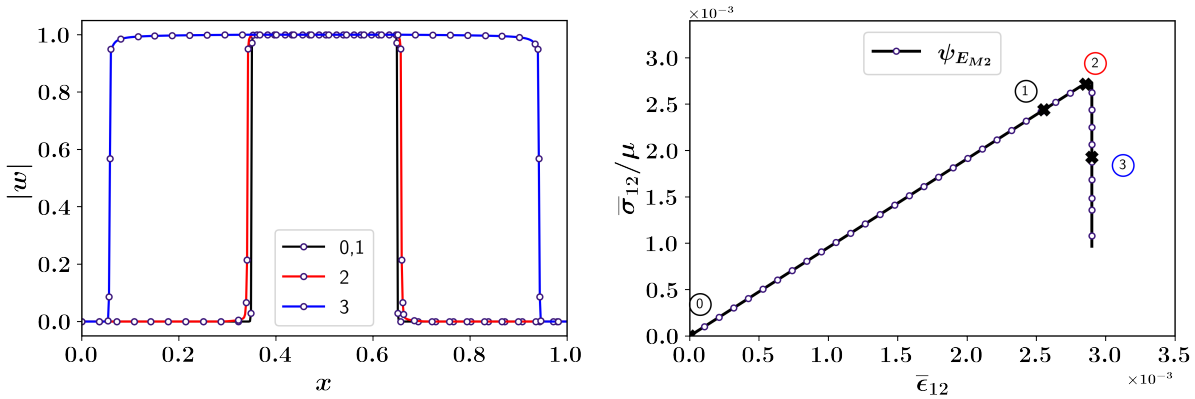

(a) (b)

Fig. 15: Crack propagation (a) and associated softening in stress-strain curve (b) representing different phases of propagation for the elastic strain energy function, $\psi_{E_{M2}}$ under mode-II loading.

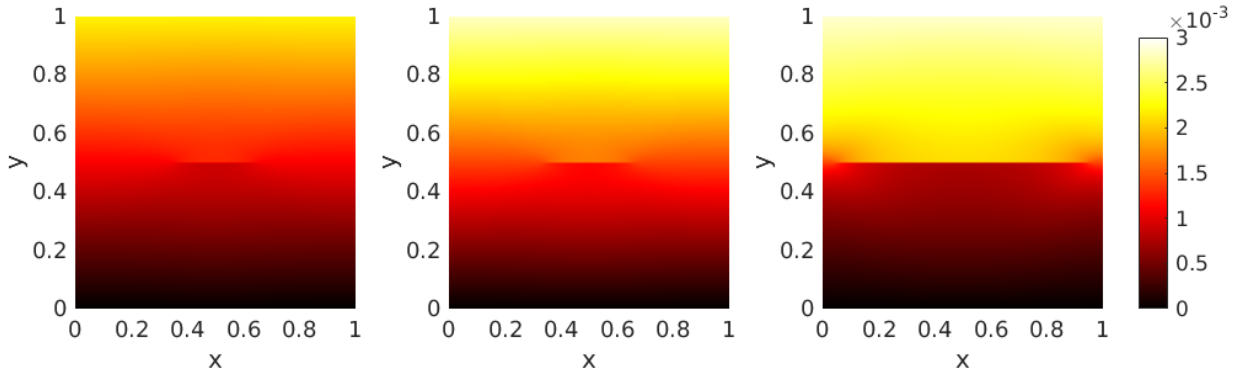

(a)

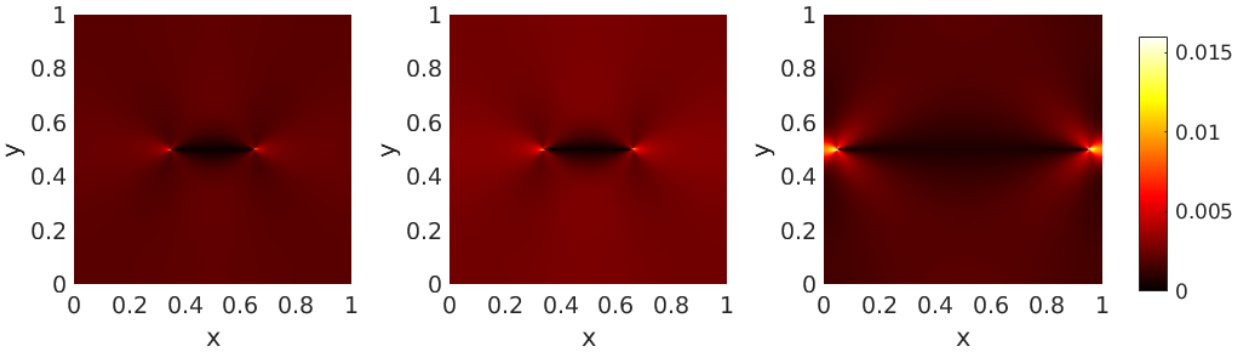

(b)

Fig. 16: Distribution of displacement u_1 (a) and stress fields σ_{12} (b) in y-direction, under mode-II loading for $\psi_{E_{M1}}$ following different phases of crack propagation in Fig. 14b from left to right.

4.2.5. Single and multiple edge cracks

The purpose of this case study is to show that the current implementation is not limited by the periodic boundary conditions associated with FFT implementation of [3]. Due to the FE framework, there is no restriction on implementing the type of initial and boundary conditions. Following Miehe *et al.* [51], the geometric setup and boundary conditions for the single edge crack specimen subjected to tensile load are shown in the Fig. 17. As detailed in [50], it is important to highlight that, the FCM model produces identical equations as phase field only with $m = 2$. But the current choice of $m = 1$ retains the gradient of the crack field in the evolution equation, Eq. (17). According to Section 5.1, Eq. (47) in [51], the Lame's parameters λ and μ are set to 121.15 KN/mm^2 and 80.77 KN/mm^2 respectively. The same values are adopted for the current FCM model as well. As shown in [51], for the phase field model the critical energy release rate g_c and length scale parameter l are 0.0027 KN/mm and 0.015 mm respectively. Thus, the non–dimensional critical energy release rate is computed as $g_c/(l\mu)$ resulting in 0.0023. For the current FCM model, a nearby value of 0.0027 is chosen for better comparison. Fig. 18 shows the comparison of stress–strain response of single edge crack with the literature [51] and a good match is observed. The displacement and stress field distributions at different instants during crack propagation are shown in Figs. 19a and 19b.

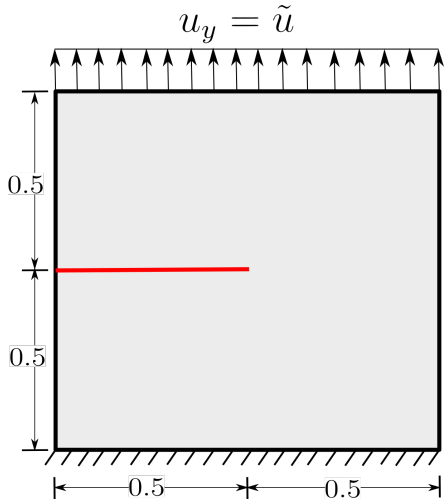

Fig. 17: Initial setup for a single edge crack specimen with boundary conditions.

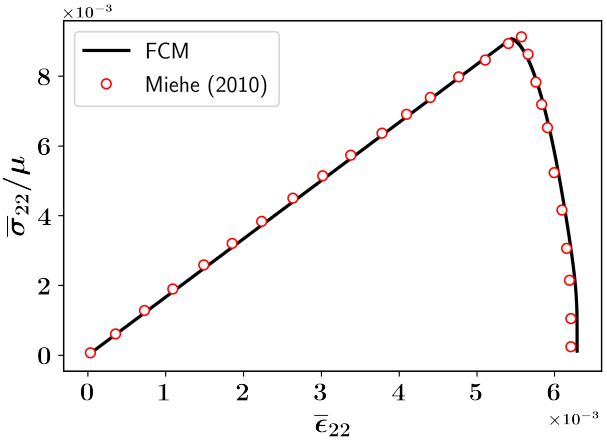

Fig. 18: Comparison of stress – strain response for an single edge notched specimen against literature [51].

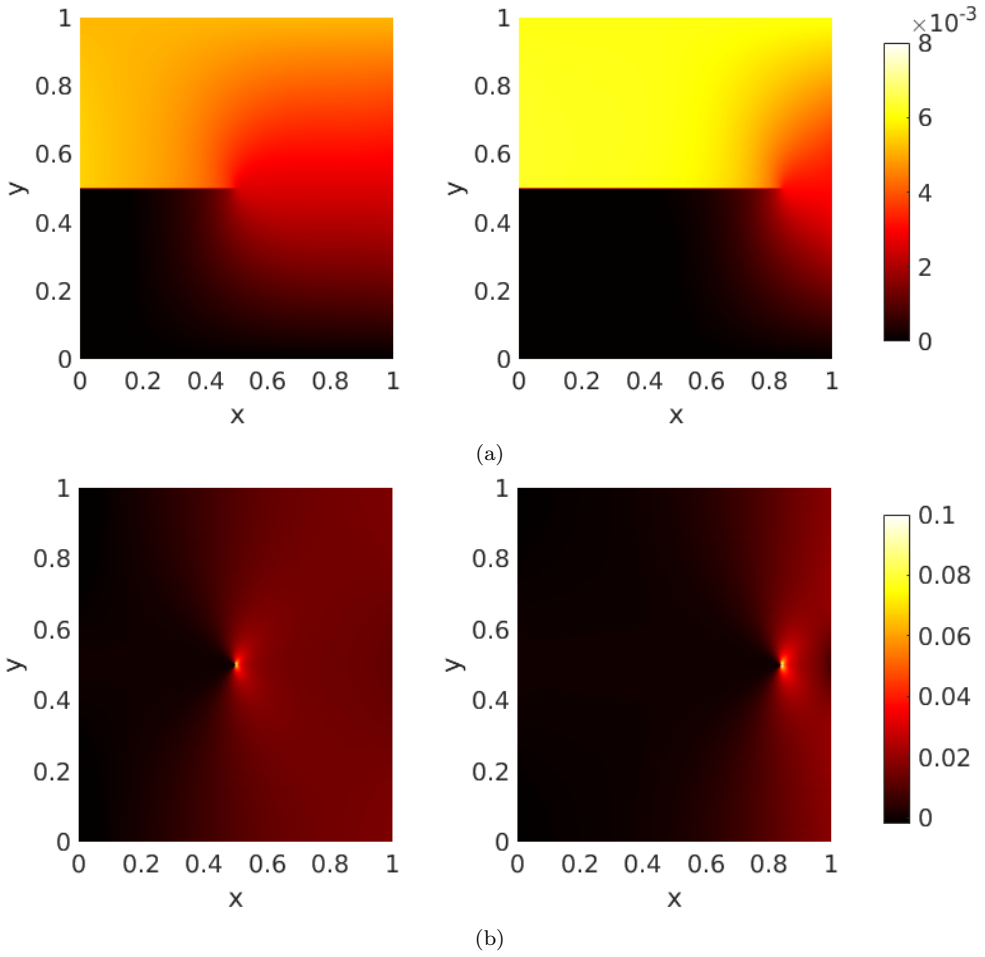

Fig. 19: Distribution of displacement u_2 (a) and stress fields, σ_{22} (b) for a single edge crack.

Depending on the relative position and orientation of the crack fields, the local stress fields are severely affected by the neighboring cracks. During the process of interaction, the adjacent cracks may magnify or diminish the stress fields. Three cracks C_1, C_2 and C_3 (see Fig. 21b) of equal width w_c are placed in three different layers. Pre–existing cracks C_1 and C_3 start from the right boundary whereas C_2 starts from the left boundary. The crack evolution and its associated stress strain response are shown in Fig. 20. The softening curve contains two softening zones where the first softening happens due to crack C_2 and the long softening zone is due to cracks C_1 and C_3 respectively. From Fig. 20 it is evident that the C_1 and C_3 crack fields influence the early motion of the crack tip of C_2. Accordingly, the displacement contours in the y direction, u_2 showing different phases in crack propagation are evident in Fig. 21a. It is interesting to observe that the entire domain is fractured into four pieces due to the presence of three parallel cracks. The respective stress contours are shown in Fig. 21b. It is clear that during the initial loading phases, the crack tip C_2 has been exposed to a higher level of stress concentration when compared to their counterparts.

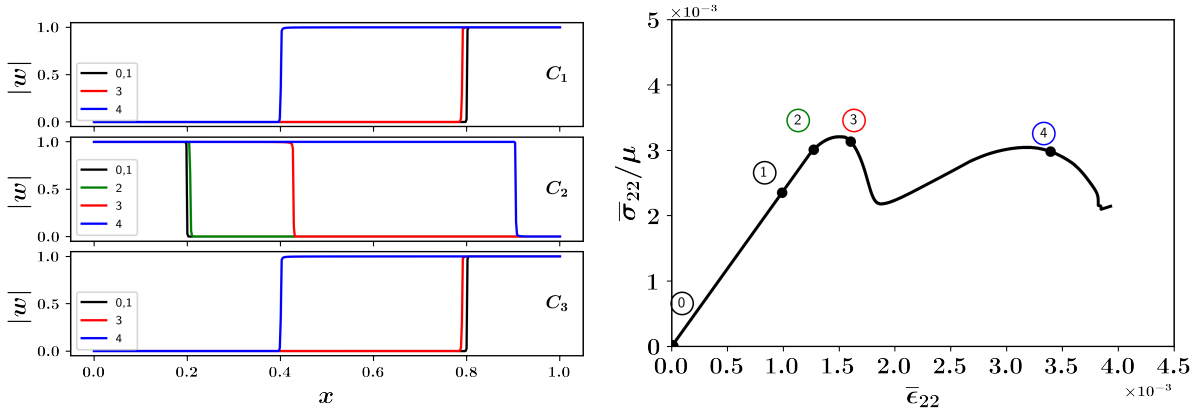

(a) (b)

Fig. 20: Crack propagation (a) and associated softening in stress-strain curve (b) representing different phases of propagation for multiple single edge cracks subjected to mode-I loading.

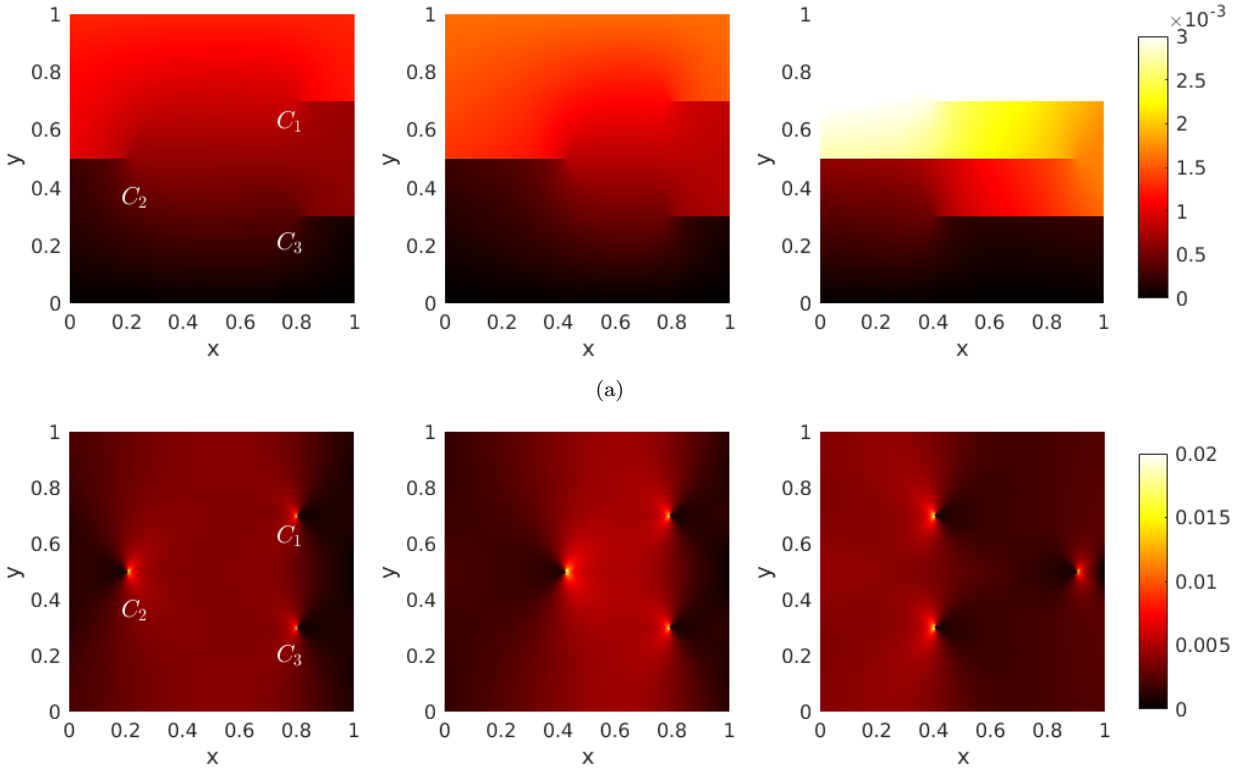

(a)

(b)

Fig. 21: Distribution of displacement u_2 (a) and stress fields σ_{22} (b) in the y-direction, for a multiple single edge cracks following different phases of crack propagation in Fig. 20 from left to right.

4.2.6. Coalescence of cracks in single planar layer

In this section, using the FCM model, the coalescence of coplanar cracks of the same width, which are placed at a finite distance s (ligament length) is demonstrated. Several micro–cracks will develop during loading and coalesce by making a large fatal crack that affects overall structural behavior. Numerous experimental and numerical studies [55, 56] also show that the crack merging process in brittle materials is imminent. Upon defining the cracks as C_1 (left) and C_2 (right), and crack tips as A,B and C,D (see Fig. 23b) different phases of crack propagation and their merging process as predicted by FCM is shown in Fig. 22.

- ⓪ – ① shows a stable linear phase with no crack motion. ① – ② shows a stable crack propagation. Beyond instant-② it shows unstable crack propagation with steep softening. Precisely at the instant ④ the merging of cracks can be observed. Later at instant ⑤ due to coalescence, a big crack is formed.

- The displacement fields in the y direction are shown in Fig. 23a. Fig. 23b shows the σ_{22} stress fields during the coalescence process. The variation of crack tip stresses (σ_{22}) for A and B crack tips is shown in Fig. 24. As the two cracks approach each other, the crack tip near the neighboring crack, i.e., crack tip 'B', experiences more stress than crack tip 'A'. (It is worth noting that a similar type of behavior for the coplanar cracks is presented in [57] where an elevation of stress intensity factors near the crack tip that is facing the neighboring crack is shown in Fig. 2.58, of Chapter–2.)

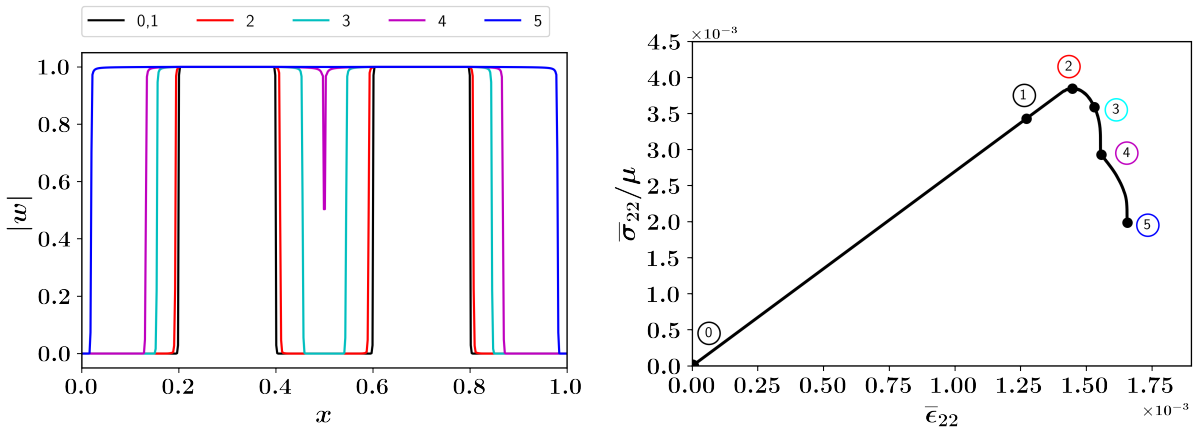

(a) (b)

Fig. 22: Crack propagation (a) and associated softening in stress-strain curve (b) representing different phases of propagation during coalescence of two cracks placed in a single planar layer when subjected to mode-I loading.

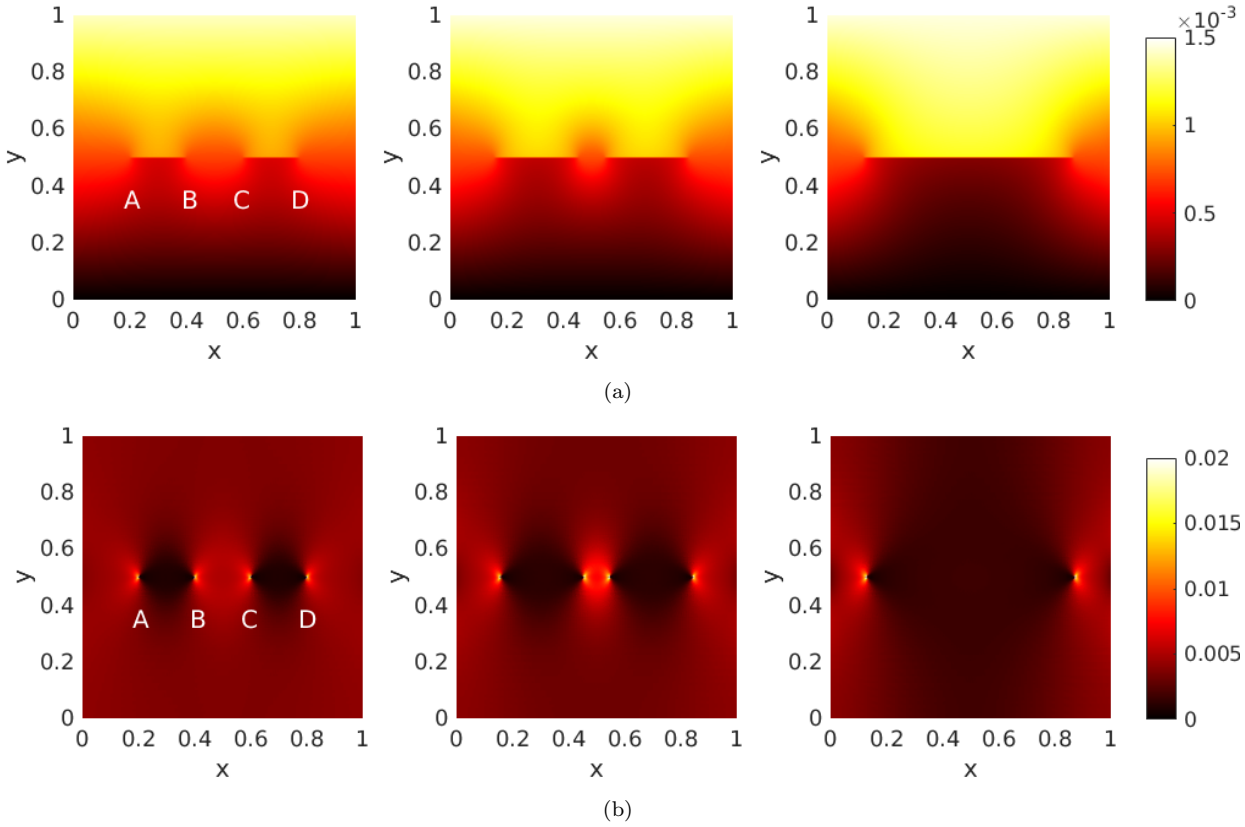

Fig. 23: Distribution of displacement u_2 (a) and stress fields σ_{22} (b) in the y-direction, during coalescence of cracks following different phases of crack propagation in Fig. 22 from left to right. Cracktips from A,B and C,D are shown in snapshot.

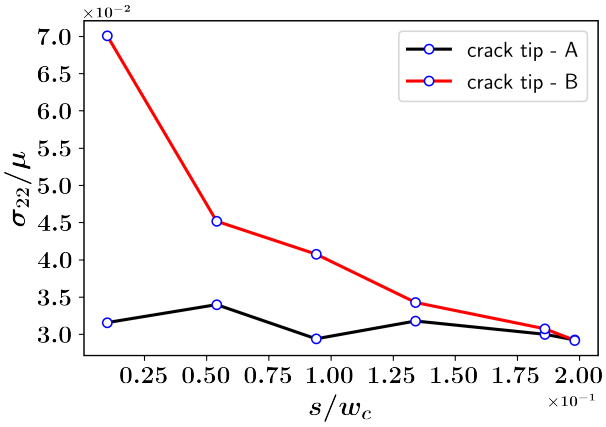

Fig. 24: Variation of crack tip stresses with the reduction in distance between the coplanar cracks.

4.3. Crack propagation under compressive loadings

According to classical fracture mechanics theory, it is believed that crack arrest is inevitable if the specimen is subjected to fully compressive loads. The compressive loads result in a zero energetic driving force on crack tips and merges the crack flanks. However, there is substantial experimental evidence to prove that cracks indeed propagate under compressive loading [58–61]. During compression, the fracture process is initiated due to locally developed tensile stresses near crack tips [62]. Unlike for tensile fracture, the brittle crack growth under compression is not responsible for the overall failure [63]. Further, in compressive loading, the extension of many micro-cracks is responsible for the catastrophic fracture. Formation of non–coplanar cracks or wing cracks [64] is a common phenomenon in uniaxial, bi/triaxial compressive loading. For an angular crack subjected to compressive loading, primary wing cracks (tensile) and secondary sliding/friction cracks emanate from the crack tips. The wing cracks try to orient themselves in the major principal compressive direction and propagate only with the external load increase. It probably explains the stress differential effect between tensile and compressive failures, where the latter requires large compressive loads for the cracks to propagate. A detailed analysis of brittle fracture using the FCM model subjected to uniaxial/biaxial compressive loads is presented in this section.

4.3.1. Biaxial compression

The present numerical experiment investigates the crack growth under biaxial compression. Many experimental pieces of evidence [59, 61, 65, 66] suggest that under biaxial compressive loadings, cracks do propagate due to the locally developed tensile stress at the crack tips. The initial setup for biaxial loading is similar to the previous case studies where a square specimen with a central crack is oriented in the x direction. In biaxial loading the specimen is subjected to compressive strains in both x and y directions ie., $(\varepsilon_{11} < 0, \varepsilon_{22} < 0)$. The compressive strain is gradually applied in the y direction, whereas in the x direction parallel to the crack axis, constant compressive strain is maintained throughout the loading. Fig. 25 shows the stress–strain curves for two different pre–strain levels as ε_{11} =0.004 and 0.005. It is interesting to note that due to the presence of ε_{11}, the initial stress is non-zero. Due to the increase in ε_{11} from 0.004 to 0.005, initial stress rises from 0.016 to 0.02, which indicates the early crack propagation. The stress fields in x direction under biaxial compression are shown in Fig. 26.

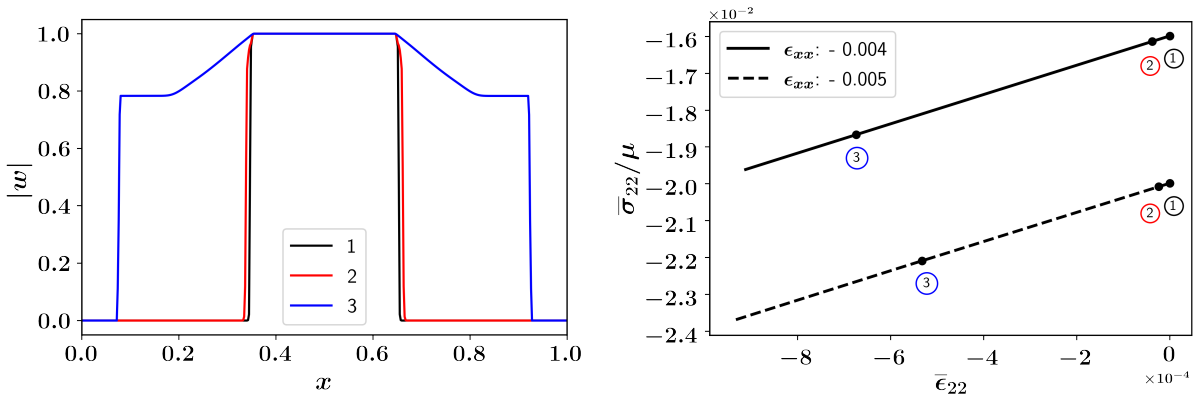

(a) (b)

Fig. 25: Crack propagation (a) and associated stress–strain curve (b) representing different phases of propagation subjected to biaxial compressive loading.

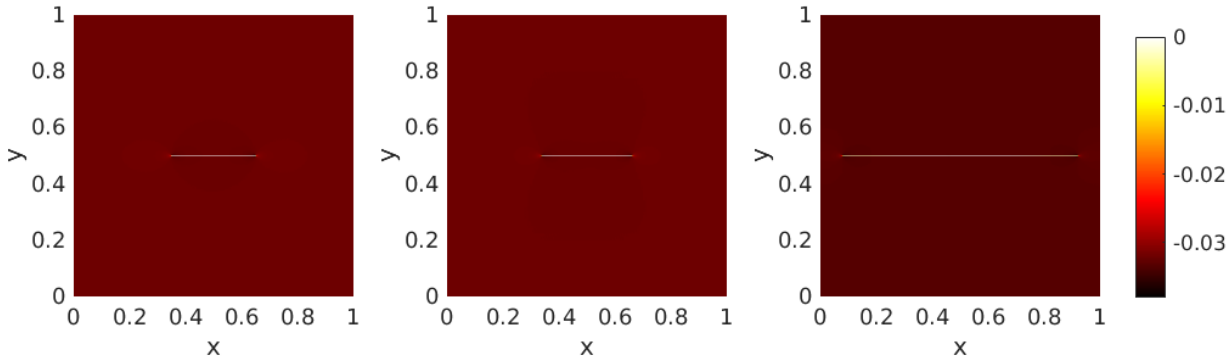

Fig. 26: Stress fields in x-direction, σ_{11} subjected to biaxial compressive loadings following different phases of crack propagation in Fig. 25 from left to right.

4.3.2. Brazilian test

Brazilian test is often referred to as indirect tensile test [59] where the crack extension happens due to Poisson's effect during compression. Similar to the experimental studies by [59], the setup for the present numerical study is shown in the Fig. 27. The setup contains a cylindrical specimen subjected to an equal magnitude of P pressure from top and bottom along the diametrical axis. To avoid rigid body motion, displacements in x and y directions are restrained at the center portion of the cylinder. The specimen radius is R, and the initial crack width is w_c. The crack is oriented vertically along the diametrical plane, with both the crack tips subjected to compressive loads.

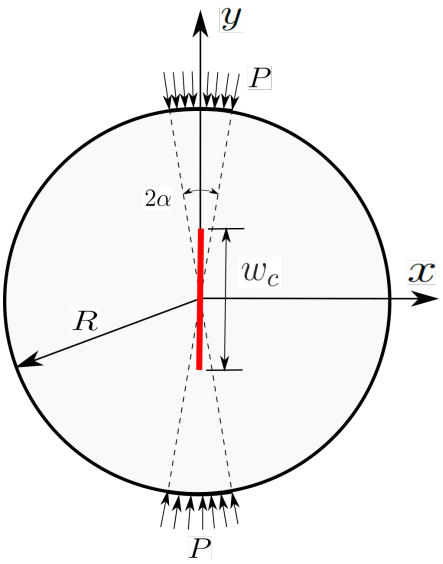

Fig. 27: Initial setup for Brazilian test with a central crack placed in the vertical postion and pressure is applied aling the diametral axis over an angle of 2α.

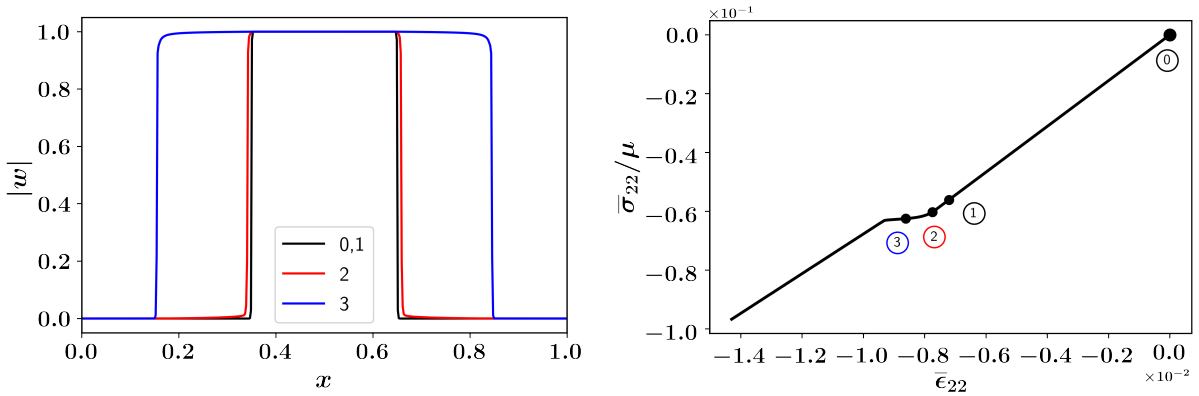

(a) (b)

Fig. 28: Crack propagation (a) and associated stress-strain curve (b) representing different phases of propagation when subjected to Brazilian test on a circular cylinder.

Various phases of crack propagation and the corresponding stress–strain curve for the Brazilian test are shown in Fig. 28. Since the crack is not oriented perpendicular to the loading direction, no steep softening in the stress–strain curve is noted. Fig. 29a shows the displacement fields in the x direction, and the splitting of the Brazilian disc along the compressive direction or the diametrical axis is observed. The stress fields in the y direction corresponding to different phases of crack propagation are shown in Fig. 29b. It is interesting to note that the stress states near the crack tips are tensile, whereas the remaining portion of the disc is compressive. The same is shown in Fig. 30 where the normal stress perpendicular to crack, i.e., σ_{11} is positive near the crack tips.

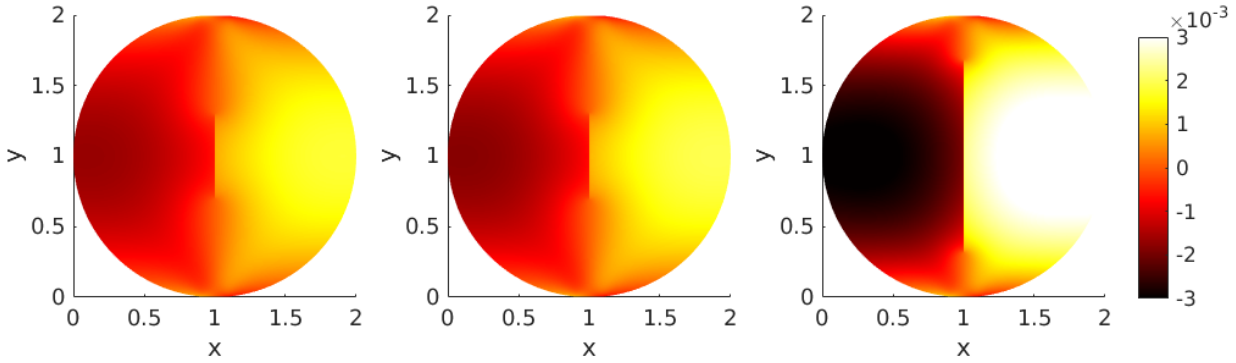

(a)

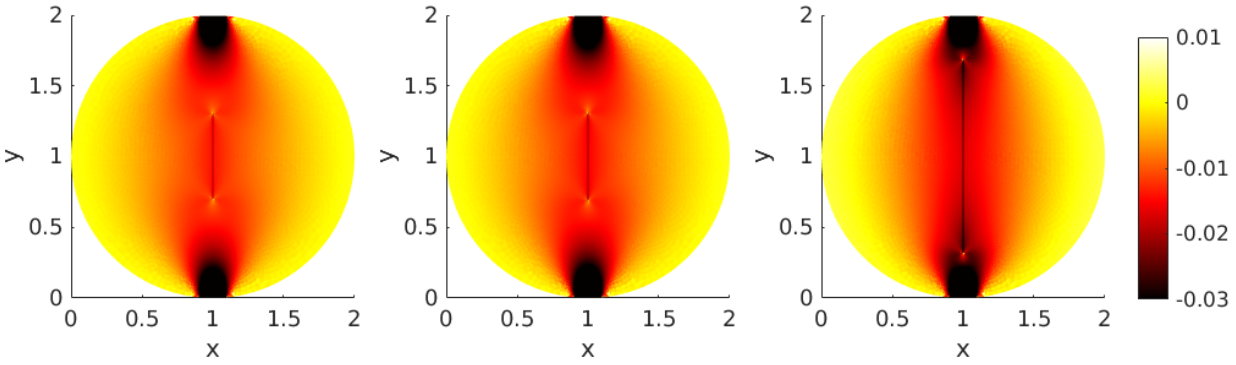

(b)

Fig. 29: Distribution of displacement u_1 (a) in the x-direction and stress field σ_{22} (b) in the y-direction, in Brazialian test following different phases of crack propagation in Fig. 28 from left to right.

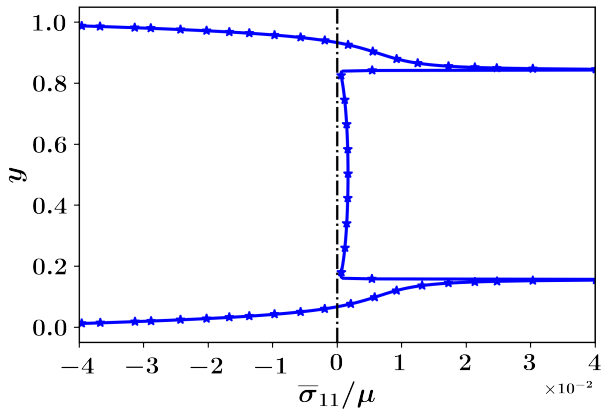

Fig. 30: Evolution of σ_{11} stress at different stages of crack propagation.

4.3.3. Three point bending test

A classical three point bending test problem which is often studied in the literature [51, 67] is presented in the current section. The initial geometric configuration and associated

boundary conditions are illustrated in Figs. 31a and 31b. Also, Figs. 31c and 31d represent the discretization of the beam using quadrilateral elements. Notably, a finely refined mesh is employed in the proximity of the crack region. Simultaneously, a displacement of $\tilde{u}$ is applied in the negative y direction at the center of the beam (see Fig. 31a). The parameters relevant to the current study are detailed in Table 1. Two cases are examined: one involving symmetric loading with a crack positioned precisely at the center of the beam, and another with an asymmetric crack offset by 0.2 units from the center line. The former corresponds to a pure mode–I loading, while the latter, with an eccentric crack, represents a mixed–mode loading.

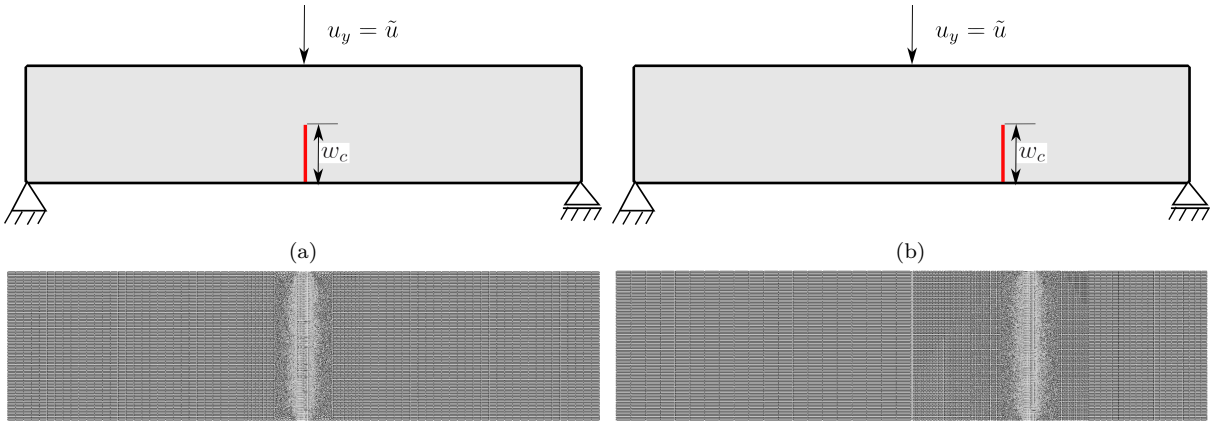

Fig. 31: Initial setup of three point bending beam with boundary conditions of (a) symmetric and (b) asymmetric crack and their respective (c), (d) geometric discretizations.

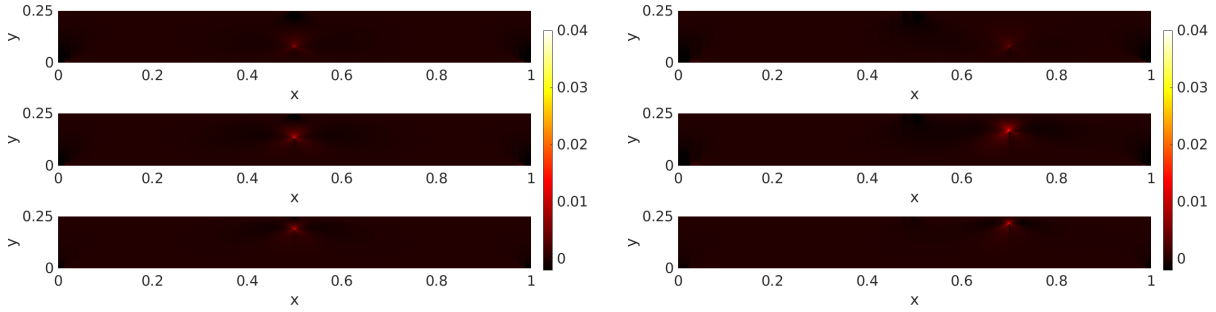

Fig. 32: Distribution of stress $\boldsymbol{\sigma}_{22}$ in a three point bending beam under (a) symmetric and (b) asymmetric crack.

The extent of the mode-II fracture contribution can be adjusted by varying the crack offset distance. The resulting crack propagation and stress distribution are shown in Fig. 32. It is noteworthy that, owing to our assumed layer model, the crack path remains confined

to the layer even in the case of an eccentric crack without any deflection due to mode-II influence. Section 2.1 discusses the main assumption behind the governing equations of the layer model. The crack field in this model (see Eq. (8)) has only one non–zero component in the crack's normal direction, restricting movement to a single layer and predicting linear trajectories. To capture crack motion beyond this layer for 2D/3D crack branching, the full governing equations with all crack field components, as shown in Eq. (1), must be addressed. The finite element approach demonstrated in Section 3.1 requires modification to accommodate these crack field components effectively. Furthermore, enhancing the current approach involves avoiding the finite difference approach for solving the layer equation. Instead, employing a finite element approach to solve both the crack field and linear momentum equations, with crack field components as finite element degrees of freedom [68]), can enhance numerical efficiency. The stress–strain curves for both symmetric and asymmetric cracks are shown in Fig. 33. It can be observed that the peak stress is higher in the case of an asymmetric crack when compared to a symmetric crack. It is worth noting that a similar type of behavior is observed in [69].

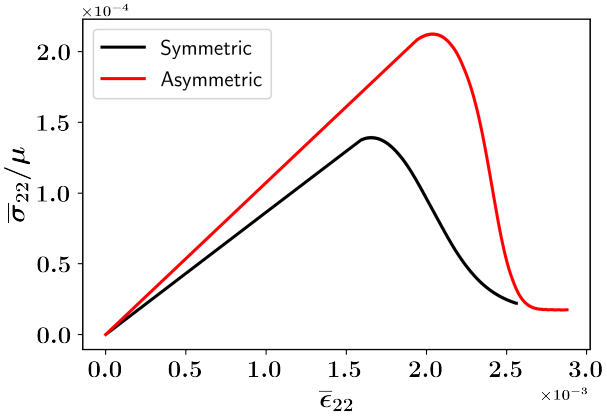

Fig. 33: Stress–strain response for a three point bending test with (a) symmetric and (b) asymmetric cracks.

4.4. Discussion on crack irreversibility

In the present section, the influence of crack energy density functions (see Fig. 2) on the healing characteristics of crack in FCM model is discussed. It is shown in Section 4.1 that in the absence of external loading, i.e., $G = 0$, the crack energy density function η_1 admits an equilibrated position for small values of ϱ maintaining sharp crack fronts. Essentially, the parameter ϱ does not indicate whether a crack heals, but only signifies the regularization of the crack tip thickness. Thus, by eliminating the effects of ϱ by assuming a value of 0.1, for η_2 (Griffith type crack energy density energy function) a similar analysis on the possible equilibrated condition is carried out, and the observations are as follows.

- Fig. 34a shows the annihilation process of crack at several time instances for the absence of external loading. Furthermore, It is evident that regardless of the ϱ value, no equilibrium position can be attained for the crack energy density energy function

η_2. The non–zero surface beyond w_2 (see Fig. 2) for η_2 helps smear out the crack completely and enforces the irreversibility constraint separately.

- However, Fig. 34b suggests that with the enforcement of crack irreversibility condition as shown in Eq. (19), the crack indeed finds a stable position. No signs of crack healing are observed with the enforcement of irreversibility condition.

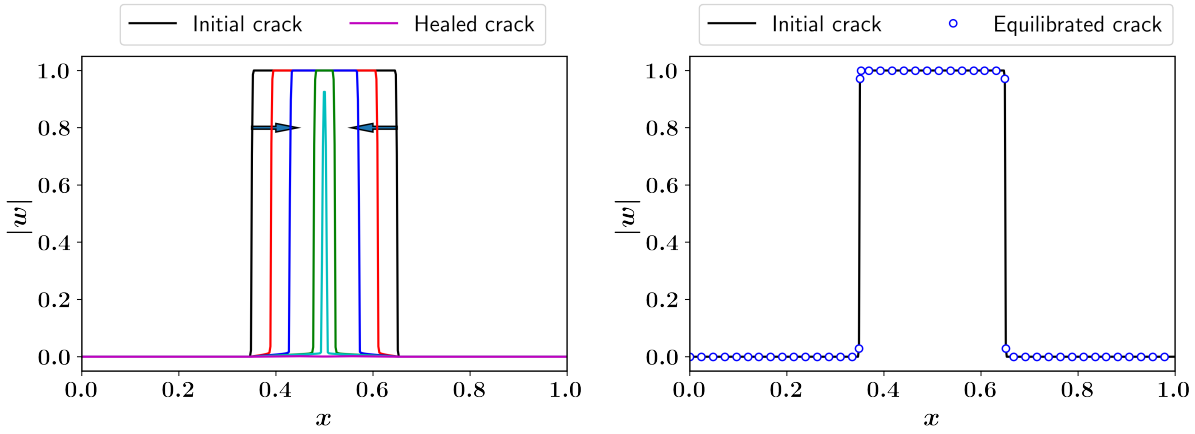

(a) (b)

Fig. 34: Crack healing observed in η_2 crack energy density function (a) without enforcing irreversibility constraint, (b) with irrversibility constraint.

- As emphasized in Section 1, the novel feature of FCM model is the inbuilt irreversibility, i.e., no need to satisfy the irreversibility constraint separately. Fig. 35 demonstrates this fact where the crack finds an equilibrated position with or without the enforcement of irreversibility condition.

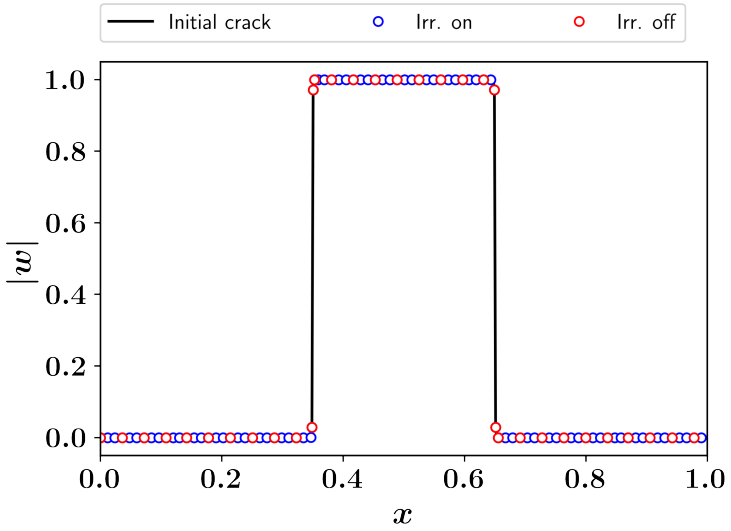

Fig. 35: Equilibrated positions of crack for η_1 crack energy density energy function with irreversibility condition on and off.

4.5. Crack propagation in ductile materials

In structural materials, ductile fracture primarily arises from the processes of void nucleation, growth, and coalescence. As mentioned in [70], void nucleation stems from the decohesion of multiphase particles, and these voids subsequently enlarge due to the plastic deformation of the matrix. Furthermore, the coalescence of voids occurs due to the localized shearing or necking between the adjacent voids [71, 72].

Recently, various models addressing the extension of phase field brittle fracture to ductile fracture in small deformation [39, 40, 73] and finite deformation regimes [74] have been proposed. Typically, in phase-field approach, the free energy function is supplied with an additional energy term for plasticity, along with elastic strain energy density and surface energy terms. Certain models, like those suggested by [39, 73], do not modify the plastic energy term based on the phase field. Conversely, in the models presented by [38, 74], a plastic degradation function influences the plastic energy function. As a result, the effectiveness of these models is significantly influenced by the coupling between phase-field and plasticity. In contrast, the current implementation does not involve any modifications to the degradation function or crack energy density functions. Instead, it employs a straightforward yet effective approach to ductile fracture.

Typically, ductile materials show hardening followed by linear elastic behavior and gradual softening, eventually leading to failure. A rate–dependent Drucker–Prager (DP) plasticity model is chosen for the present study, as detailed in Section 3.2. Various parameters involved in the plasticity model are given in Table 2. The parameters α and α_ψ, which include the effect of pressure, are considered to be zero. Effectively, the DP plasticity reduces the conventional J_2 plasticity. To mimic the rate–independent behavior, the rate sensitivity parameter $m = 0.02$ is chosen to be very small. The drag parameter $B_m = 0.01$ is maintained the same as in the case of brittle fracture.

Table 2: Material parameters for ductile fracture.

B_m	m	α	α_ψ
0.01	0.02	0.0	0.0

To simulate the effect of plasticity in crack propagation, an identical setup for brittle fracture, as shown in Section 4.2.1, subjected to mode-I loading is chosen. Additionally, linear isotropic hardening (see Eq. (43)) with parameters hardening constant $\mathcal{H} = 0.2$ and the non–dimensional yield value $\sigma_{yo} = 0.002$ are considered.

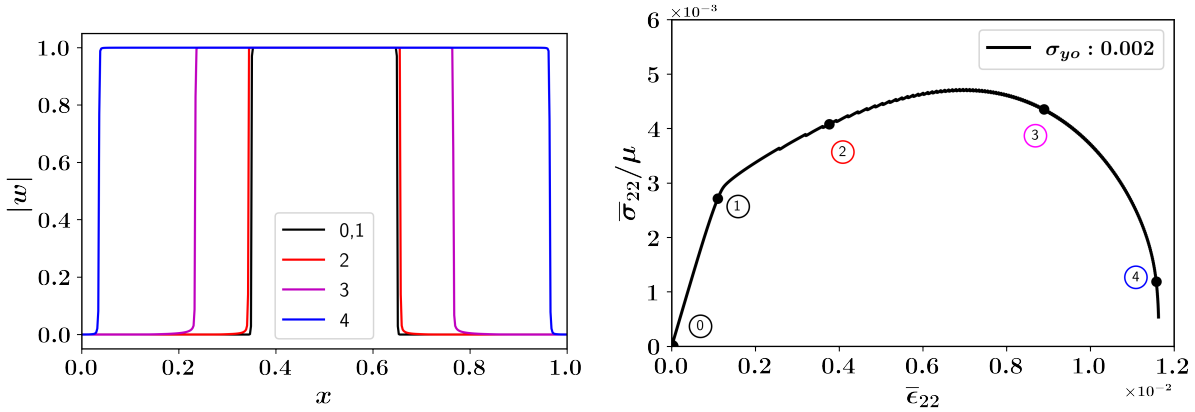

(a) (b)

Fig. 36: Crack propagation (a) and associated stress–strain curve (b) representing different phases of propagation when subjected to mode-I tensile loading for the case of ductile fracture with hardening.

The crack propagation and the associated ductile stress–strain curve is shown in Fig. 36. It can be observed that similar to brittle fracture, the crack propagation during ductile failure also passes through different phases before failure. The observations are as follows

1. Initially, from ⓪–① represents the linear phase where no crack propagation occurs.

2. The linear regime is followed by a hardening zone from ①–② where the specimen strengthens with hardening. No crack motion is visible in this phase also. When the applied strain reaches the instant ②, the energy supplied exceeds the magnitude of surface. It results in a net driving force on the crack.

3. Beyond ②, the motion of the crack is accompanied by the hardening until the strain reaches 0.07. Later, a gradual softening happens from ③–④ and finally, the specimen fails at instant ④.

4. The displacement fields u_2 at different snapshots of crack motion are shown in Fig. 37. The components of stress and plastic strain fields in the y direction are shown in Figs. 38a and 38b respectively. It is evident that the plastic strain fields are forceful

near the crack tips and slowly spread to the neighboring regions as the crack propagates.

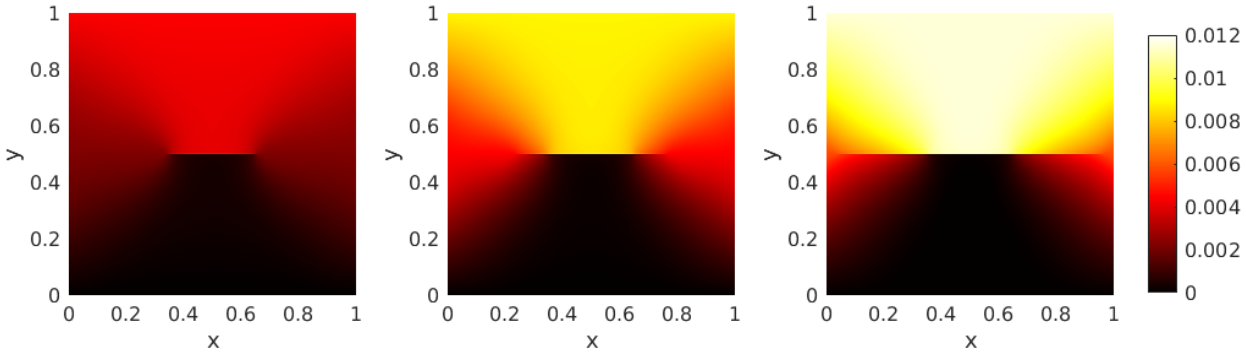

Fig. 37: Displacement fields in the y-direction, u_2 under mode-I loading for ductile fracture. The displacement fields are related to the crack propagation at snapshots ②, ③ and ④ respectively.

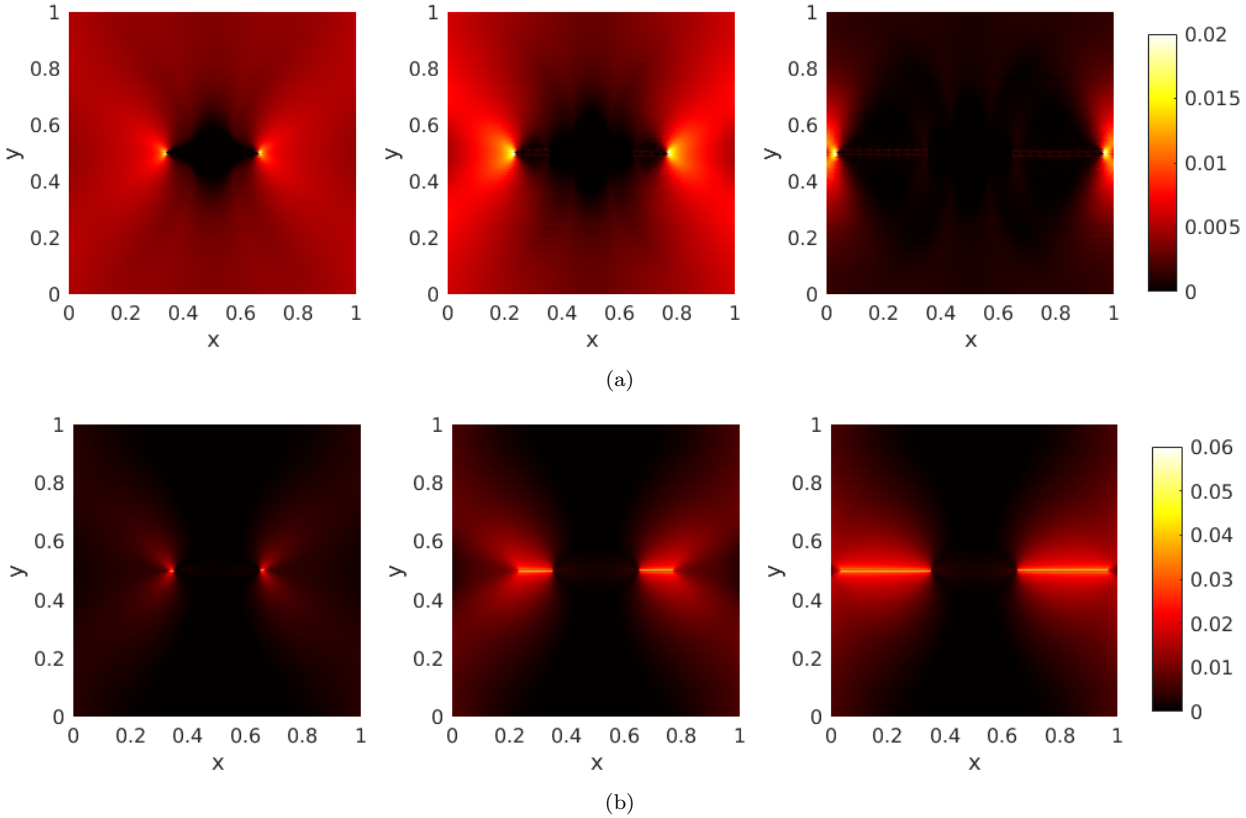

Fig. 38: Distribution of stress σ_{22} (a) and plastic strain field ε_{22} (b) in the y-direction, under mode-I loading for ductile fracture.The displacement fields are related to the crack propagation at snapshots ②, ③ and ④ respectively.

4.6. Sensitivity analysis

In the present section, the impact of different parameters such as yield strength $\boldsymbol{\sigma}_{yo}$, friction angle β, and hardening constant $\mathcal{H}$, is presented. A square domain, featuring a pre-existing central crack (see Fig. 1), is subjected to mode-I loading. As discussed in Section 4.1, the crack is equilibrated before the loading is applied. Fig. 39 illustrates the stress–strain response to varying values of the parameters $\boldsymbol{\sigma}_{yo}$ (ranging from 0.001 to 0.003), β (ranging from 0 to 30°), and $\mathcal{H}$ (ranging from 0.1 to 0.3), while the remaining parameters are held constant. The corresponding crack motion at a fixed applied strain ($\overline{\boldsymbol{\varepsilon}}_{22} = 0.08$ for $\boldsymbol{\sigma}_{yo}$ & $\mathcal{H}$, and $\overline{\boldsymbol{\varepsilon}}_{22} = 0.125$ for $\beta = 0.125$) is presented in Fig. 40. Elevated values of yield stress and hardening constants impart the crack with greater energy, resulting in swifter motion. This also leads to a more rapid softening response in the stress-strain curve. The behavior is also evident in Figs. 39a and 39b where the blue curves, representing higher yield stress ($\boldsymbol{\sigma}_{yo} = 0.003$) and hardening constant ($\mathcal{H} = 0.3$) exhibit a quick softening stress–strain response. The corresponding crack motion is shown in Figs. 40a and 40b. On the contrary, as the friction angle increases, there is a rise in the magnitude of plastic strains, leading to a slower response in crack motion. This trend is evident in Fig. 39c, where the black curve (with a lower friction angle of $\beta = 0°$) experiences rapid softening in comparison to the blue curve ($\beta = 30°$), which corresponds to the highest friction angle. The corresponding variation in crack movement under a constant applied strain of $\overline{\boldsymbol{\varepsilon}}_{22} = 0.125$ with different friction angles is shown in Fig. 40c.

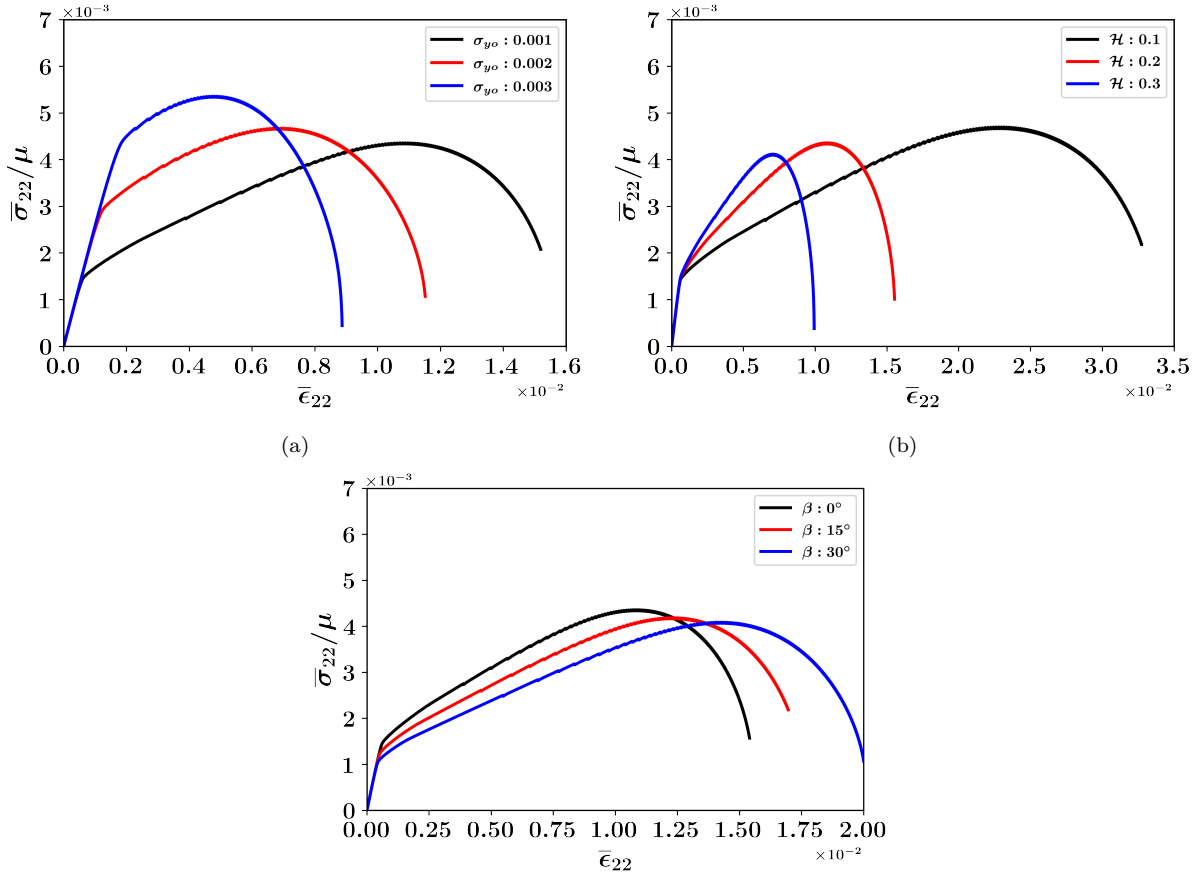

Fig. 39: Influence of (a) yield stress, (b) hardening constant, and (c) friction angle on stress–strain curve.

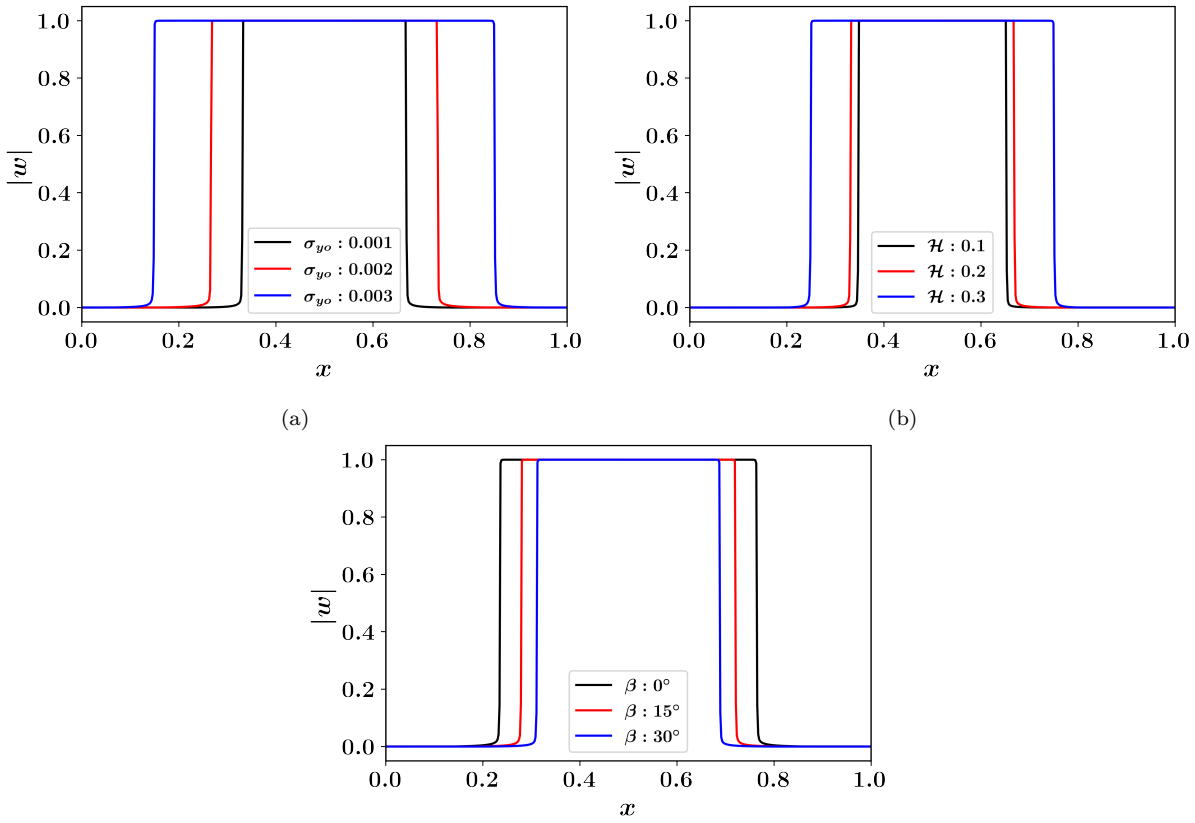

Fig. 40: Schematic showing the crack propagation under the influence of (a) yield stress (at $\overline{\varepsilon}_{22} = 0.08$), (b) hardening constant (at $\overline{\varepsilon}_{22} = 0.08$) and (c) friction angle (@ $\overline{\varepsilon}_{22} = 0.125$).

Overall, in this work, a crack evolution equation is solved using the upwinding finite difference technique and the balance of linear momentum with a finite element framework. Several benchmark tests are illustrated, including mode-I/II loading on central and edge cracks, assessments of crack coalescence, and investigations of crack propagation under compressive loading for brittle fracture. Additionally, mode-I loading for ductile fracture is also demonstrated. It is established that the current implementation of FCM can reproduce the essential features of classical fracture mechanics. These preliminary investigations on the FCM model restricted to a single fault layer give us a fundamental insight into the model's basic capabilities. It is worth emphasizing that in Section 2.1, the primary assumption underlying the development of governing equations for the layer model is discussed. The vectorial crack field in the layer model (see Eq. (8)) exhibits only one non-zero component in the normal direction of the crack. Consequently, this constrains the crack's movement to a single layer, resulting in the limitation of the current implementation to predicting linear trajectories. However, it is important to note that this represents a simplified scenario compared to the complex governing equations outlined in Eq. (1), which are designed to capture full 3D and non-linear crack trajectories. Although the current implementation has limitations, such as crack propagation is restricted to a single fault layer, it is shown in the

present study that many paradigmatic problems related to classical fracture mechanics can be solved with reasonable accuracy. Nevertheless, implementing a full field crack evolution law in 3D without any restrictions to a layer is of immediate importance. While the current implementation of ductile fracture exhibits fundamental features of metal plasticity, it is important to note the existence of a comprehensive FCM framework that considers the effects of porosity evolution on degrading moduli, as described in [4]. We look forward to future studies exploring this aspect in greater detail. Additionally, the exploration of dynamic crack propagation within the current numerical framework is left for future studies.

5. Conclusions

Numerical implementation of a novel rate–dependent field crack mechanics based model for fracture is demonstrated. Proposed by Acharya [2] for brittle fracture, and implemented for 3–D by Morin and Acharya [3], the present work extends it to ductile fracture as well. A few important results are summarized in the following.

1. The model captures different phases of crack propagation, such as stable and unstable crack propagation for various loading conditions. The model predicts the threshold stress for the crack motion, which is similar to the Peierls stress associated with dislocation motion.

2. A special feature of the FCM model is the regularization of the crack tip by Laplacian term. A detailed study about the effect of the parameter $\varrho = \kappa/a$ (ratio of crack–tip energy density and the magnitude of crack energy density) that regulates the crack tip is also discussed.

3. The present variant of the FCM model is inherently rate–dependent, and the parameter B_m controls the drag related to the crack motion. The sensitivity of the crack propagation under the influence of B_m is also discussed. It is shown that as $B_m \to 0$, the rate–independent limit is achieved.

4. Another remarkable characteristic of the FCM model is that the crack irreversibility is a built–in phenomenon. In this context, it is shown that the model can utilize a variety of crack energy density functions, and if it is zero surface energy, no extra irreversibility constraint is required. In contrast, if the surface energy function contains a finite value behind the crack tip (like Griffith's case), then only irreversibility must be satisfied.

5. Extension of brittle fracture to ductile is a straightforward process, and a rate–dependent, pressure–sensitive, Drucker–Prager plasticity is coupled with the current implementation. It is shown that the developed model can predict the ductile fracture when subjected to mode-I loading. The retardation of the crack propagation due to plastic strains is also shown.

Acknowledgment

AA acknowledges the financial support provided by IIT Bombay for Ph.D. student BVSSB. AA and BVSSB also acknowledge discussion with Prof. Amit Acharya (CMU, USA) and a critical review of the formulation and manuscript without which this outcome would have not been possible.

Conflict of Interest

The authors have no relevant financial or non-financial interests to disclose.

References

[1] Alan Arnold Griffith. Vi. the phenomena of rupture and flow in solids. Philosophical transactions of the royal society of london. Series A, containing papers of a mathematical or physical character, 221 (582-593):163–198, 1921.

[2] Amit Acharya. Fracture and singularities of the mass-density gradient field. Journal of Elasticity, 132 (2):243–260, 2018.

[3] Léo Morin and Amit Acharya. Analysis of a model of field crack mechanics for brittle materials. Computer Methods in Applied Mechanics and Engineering, 386:114061, 2021.

[4] Amit Acharya. A possible link between brittle and ductile failure by viewing fracture as a topological defect. Comptes Rendus. Mécanique, 348(4):275–284, 2020.

[5] Donald S Dugdale. Yielding of steel sheets containing slits. Journal of the Mechanics and Physics of Solids, 8(2):100–104, 1960.

[6] Grigory Isaakovich Barenblatt. The mathematical theory of equilibrium cracks in brittle fracture. Advances in applied mechanics, 7:55–129, 1962.

[7] Alberto Carpinteri, Silvio Valente, and P Bocca. Mixed mode cohesive crack propagation. In Proceedings of The 7th International Conference On Fracture (ICF7), pages 2243–2257. Elsevier, 1989.

[8] Arne Hillerborg, Mats Modéer, and P-E Petersson. Analysis of crack formation and crack growth in concrete by means of fracture mechanics and finite elements. Cement and concrete research, 6(6): 773–781, 1976.

[9] Huang Yuan, Guoyu Lin, and Alfred Cornec. Verification of a cohesive zone model for ductile fracture. 1996.

[10] A Needleman. An analysis of tensile decohesion along an interface. Journal of the Mechanics and Physics of Solids, 38(3):289–324, 1990.

[11] Hanen Amor, Jean-Jacques Marigo, and Corrado Maurini. Regularized formulation of the variational brittle fracture with unilateral contact: Numerical experiments. Journal of the Mechanics and Physics of Solids, 57(8):1209–1229, 2009.

[12] Natarajan Sukumar, Nicolas Moës, Brian Moran, and Ted Belytschko. Extended finite element method for three-dimensional crack modelling. International journal for numerical methods in engineering, 48 (11):1549–1570, 2000.

[13] Nicolas Moës and Ted Belytschko. Extended finite element method for cohesive crack growth. Engineering fracture mechanics, 69(7):813–833, 2002.

[14] M Stolarska, David L Chopp, Nicolas Moës, and Ted Belytschko. Modelling crack growth by level sets in the extended finite element method. International journal for numerical methods in Engineering, 51 (8):943–960, 2001.

[15] Jens M Melenk and Ivo Babuška. The partition of unity finite element method: basic theory and applications. Computer methods in applied mechanics and engineering, 139(1-4):289–314, 1996.

[16] C Armando Duarte and J Tinsley Oden. H-p clouds—an h-p meshless method. Numerical Methods for Partial Differential Equations: An International Journal, 12(6):673–705, 1996.

[17] Ted Belytschko, Lei Gu, and YY Lu. Fracture and crack growth by element free galerkin methods. Modelling and Simulation in Materials Science and Engineering, 2(3A):519, 1994.
[18] Ted Belytschko, YY Lu, and L Gu. Crack propagation by element-free galerkin methods. Engineering Fracture Mechanics, 51(2):295–315, 1995.
[19] Ted Belytschko and Tom Black. Elastic crack growth in finite elements with minimal remeshing. International journal for numerical methods in engineering, 45(5):601–620, 1999.
[20] Nicolas Moës, John Dolbow, and Ted Belytschko. A finite element method for crack growth without remeshing. International journal for numerical methods in engineering, 46(1):131–150, 1999.
[21] Robert A Gingold and Joseph J Monaghan. Smoothed particle hydrodynamics: theory and application to non-spherical stars. Monthly notices of the royal astronomical society, 181(3):375–389, 1977.
[22] Joe J Monaghan. Smoothed particle hydrodynamics. Annual review of astronomy and astrophysics, 30 (1):543–574, 1992.
[23] BN Rao and S Rahman. A coupled meshless-finite element method for fracture analysis of cracks. International Journal of Pressure Vessels and Piping, 78(9):647–657, 2001.
[24] Stewart A Silling and Ebrahim Askari. A meshfree method based on the peridynamic model of solid mechanics. Computers & structures, 83(17-18):1526–1535, 2005.
[25] Stewart A Silling, M Epton, Olaf Weckner, Jifeng Xu, and E23481501120 Askari. Peridynamic states and constitutive modeling. Journal of elasticity, 88(2):151–184, 2007.
[26] Stewart A Silling and Richard B Lehoucq. Peridynamic theory of solid mechanics. Advances in applied mechanics, 44:73–168, 2010.
[27] Robert Lipton. Dynamic brittle fracture as a small horizon limit of peridynamics. Journal of Elasticity, 117(1):21–50, 2014.
[28] Ting Zhang and Xiaoping Zhou. A modified axisymmetric ordinary state-based peridynamics with shear deformation for elastic and fracture problems in brittle solids. European Journal of Mechanics-A/Solids, 77:103810, 2019.
[29] Xin Lai, Lisheng Liu, Shaofan Li, Migbar Zeleke, Qiwen Liu, and Zhen Wang. A non-ordinary state-based peridynamics modeling of fractures in quasi-brittle materials. International Journal of Impact Engineering, 111:130–146, 2018.
[30] Md Masiur Rahaman, Pranesh Roy, Debasish Roy, and JN Reddy. A peridynamic model for plasticity: micro-inertia based flow rule, entropy equivalence and localization residuals. Computer methods in applied mechanics and engineering, 327:369–391, 2017.
[31] Erdogan Madenci and Selda Oterkus. Ordinary state-based peridynamics for plastic deformation according to von mises yield criteria with isotropic hardening. Journal of the Mechanics and Physics of Solids, 86:192–219, 2016.
[32] Martin Kružík, Carlos Mora-Corral, and Ulisse Stefanelli. Quasistatic elastoplasticity via peridynamics: existence and localization. Continuum Mechanics and Thermodynamics, 30(5):1155–1184, 2018.
[33] Gilles A Francfort and J-J Marigo. Revisiting brittle fracture as an energy minimization problem. Journal of the Mechanics and Physics of Solids, 46(8):1319–1342, 1998.
[34] Gianni Dal Maso, Gilles A Francfort, and Rodica Toader. Quasistatic crack growth in nonlinear elasticity. Archive for Rational Mechanics and Analysis, 176(2):165–225, 2005.
[35] Blaise Bourdin, Gilles A Francfort, and Jean-Jacques Marigo. Numerical experiments in revisited brittle fracture. Journal of the Mechanics and Physics of Solids, 48(4):797–826, 2000.
[36] Luigi Ambrosio and Vincenzo Maria Tortorelli. On the approximation of free discontinuity problems. 1992.
[37] Christian Miehe, Fabian Welschinger, and Martina Hofacker. Thermodynamically consistent phase-field models of fracture: Variational principles and multi-field fe implementations. International journal for numerical methods in engineering, 83(10):1273–1311, 2010.
[38] Christian Miehe, M Hofacker, L-M Schänzel, and Fadi Aldakheel. Phase field modeling of fracture in multi-physics problems. part ii. coupled brittle-to-ductile failure criteria and crack propagation in thermo-elastic–plastic solids. Computer Methods in Applied Mechanics and Engineering, 294:486–522, 2015.

[39] Fernando P Duda, Angel Ciarbonetti, Pablo J Sánchez, and Alfredo E Huespe. A phase-field/gradient damage model for brittle fracture in elastic–plastic solids. International Journal of Plasticity, 65:269–296, 2015.
[40] Roberto Alessi, Jean-Jacques Marigo, and Stefano Vidoli. Gradient damage models coupled with plasticity: variational formulation and main properties. Mechanics of Materials, 80:351–367, 2015.
[41] Michele Caputo and Mauro Fabrizio. Damage and fatigue described by a fractional derivative model. Journal of Computational Physics, 293:400–408, 2015.
[42] Giovambattista Amendola, Mauro Fabrizio, and JM Golden. Thermomechanics of damage and fatigue by a phase field model. Journal of Thermal Stresses, 39(5):487–499, 2016.
[43] JL Boldrini, EA Barros de Moraes, LR Chiarelli, FG Fumes, and ML3574980 Bittencourt. A non-isothermal thermodynamically consistent phase field framework for structural damage and fatigue. Computer Methods in Applied Mechanics and Engineering, 312:395–427, 2016.
[44] Fan Fei and Jinhyun Choo. A phase-field method for modeling cracks with frictional contact. International Journal for Numerical Methods in Engineering, 121(4):740–762, 2020.
[45] Christopher J Larsen, Christoph Ortner, and Endre Süli. Existence of solutions to a regularized model of dynamic fracture. Mathematical Models and Methods in Applied Sciences, 20(07):1021–1048, 2010.
[46] Martina Hofacker and Christian Miehe. Continuum phase field modeling of dynamic fracture: variational principles and staggered fe implementation. International journal of fracture, 178(1):113–129, 2012.
[47] Michael J Borden, Clemens V Verhoosel, Michael A Scott, Thomas JR Hughes, and Chad M Landis. A phase-field description of dynamic brittle fracture. Computer Methods in Applied Mechanics and Engineering, 217:77–95, 2012.
[48] Gergely Molnár, Aurélien Doitrand, Rafaël Estevez, and Anthony Gravouil. Toughness or strength. regularization in phase-field fracture explained by the coupled criterion. Theoretical and Applied Fracture Mechanics, 109:102736, 2020.
[49] Patrick R Amestoy, Iain S Duff, Jean-Yves L'Excellent, and Jacko Koster. Mumps: a general purpose distributed memory sparse solver. In International Workshop on Applied Parallel Computing, pages 121–130. Springer, 2000.
[50] Xiaohan Zhang, Amit Acharya, Noel J Walkington, and Jacobo Bielak. A single theory for some quasi-static, supersonic, atomic, and tectonic scale applications of dislocations. Journal of the Mechanics and Physics of Solids, 84:145–195, 2015.
[51] Christian Miehe, Martina Hofacker, and Fabian Welschinger. A phase field model for rate-independent crack propagation: Robust algorithmic implementation based on operator splits. Computer Methods in Applied Mechanics and Engineering, 199(45-48):2765–2778, 2010.
[52] Amit Das, Amit Acharya, Johannes Zimmer, and Karsten Matthies. Can equations of equilibrium predict all physical equilibria. a case study from field dislocation mechanics. Mathematics and Mechanics of Solids, 18(8):803–822, 2013.
[53] Harold M Westergaard. Bearing pressures and cracks: Bearing pressures through a slightly waved surface or through a nearly flat part of a cylinder, and related problems of cracks. 1939.
[54] Dominique Leguillon. Strength or toughness. a criterion for crack onset at a notch. European Journal of Mechanics-A/Solids, 21(1):61–72, 2002.
[55] CA Tang and SQ Kou. Crack propagation and coalescence in brittle materials under compression. Engineering Fracture Mechanics, 61(3-4):311–324, 1998.
[56] Shuwei Zhou, Xiaoying Zhuang, Hehua Zhu, and Timon Rabczuk. Phase field modelling of crack propagation, branching and coalescence in rocks. Theoretical and Applied Fracture Mechanics, 96: 174–192, 2018.
[57] Ted L Anderson. Fracture mechanics: fundamentals and applications. CRC press, 2017.
[58] Hadi Haeri, Kourosh Shahriar, Mohammad Fatehi Marji, and Parviz Moarefvand. Experimental and numerical study of crack propagation and coalescence in pre-cracked rock-like disks. International Journal of Rock Mechanics and Mining Sciences, 67:20–28, 2014.
[59] JC Jaeger and ER Hoskins. Rock failure under the confined brazilian test. Journal of Geophysical

research, 71(10):2651–2659, 1966.
[60] Antonio Bobet and HH Einstein. Fracture coalescence in rock-type materials under uniaxial and biaxial compression. International Journal of Rock Mechanics and Mining Sciences, 35(7):863–888, 1998.
[61] Evert Hoek and ZT Bieniawski. Brittle fracture propagation in rock under compression. International Journal of Fracture Mechanics, 1(3):137–155, 1965.
[62] WF Brace and EG Bombolakis. A note on brittle crack growth in compression. Journal of Geophysical Research, 68(12):3709–3713, 1963.
[63] Paul S Steif. Crack extension under compressive loading. Engineering Fracture Mechanics, 20(3): 463–473, 1984.
[64] AV Dyskin, E Sahouryeh, RJ Jewell, H Joer, and KB Ustinov. Influence of shape and locations of initial 3-d cracks on their growth in uniaxial compression. Engineering Fracture Mechanics, 70(15): 2115–2136, 2003.
[65] E Sahouryeh, AV Dyskin, and LN Germanovich. Crack growth under biaxial compression. Engineering Fracture Mechanics, 69(18):2187–2198, 2002.
[66] Hongyu Wang, Arcady Dyskin, Elena Pasternak, and Phil Dight. 3d crack growth in biaxial compression: influence of shape and inclination of initial cracks. Rock Mechanics and Rock Engineering, 53(7): 3161–3183, 2020.
[67] CHRISTIAN Miehe and ERCAN Gürses. A robust algorithm for configurational-force-driven brittle crack propagation with r-adaptive mesh alignment. International Journal for Numerical Methods in Engineering, 72(2):127–155, 2007.
[68] Rajat Arora, Xiaohan Zhang, and Amit Acharya. Finite element approximation of finite deformation dislocation mechanics. Computer Methods in Applied Mechanics and Engineering, 367:113076, 2020.
[69] Awais Ahmed, Yue Liu, T Tafsirojjaman, Aizaz Ahmad, Mudassir Iqbal, et al. Phase field model for mixed mode fracture in concrete. Engineering Fracture Mechanics, page 109439, 2023.
[70] Ahmed Amine Benzerga, Jean-Baptiste Leblond, Alan Needleman, and Viggo Tvergaard. Ductile failure modeling. International Journal of Fracture, 201:29–80, 2016.
[71] WM Garrison Jr and NR Moody. Ductile fracture. Journal of Physics and Chemistry of Solids, 48(11): 1035–1074, 1987.
[72] Viggo Tvergaard. Material failure by void growth to coalescence. Advances in applied Mechanics, 27: 83–151, 1989.
[73] Marreddy Ambati, Tymofiy Gerasimov, and Laura De Lorenzis. Phase-field modeling of ductile fracture. Computational Mechanics, 55:1017–1040, 2015.
[74] Michael J Borden, Thomas JR Hughes, Chad M Landis, Amin Anvari, and Isaac J Lee. A phase-field formulation for fracture in ductile materials: Finite deformation balance law derivation, plastic degradation, and stress triaxiality effects. Computer Methods in Applied Mechanics and Engineering, 312:130–166, 2016.

Appendix A.

For completeness the derivation of the dissipation shown in Eq. (5) is provided here. As mentioned in Section 1, the free energy density function is given as

$$\psi(\boldsymbol{\varepsilon}^e, \mathbf{c}, \mathrm{curl}(\mathbf{c})) = \psi_E(\boldsymbol{\varepsilon}^e, \mathbf{c}) + \varphi(\mathbf{c}, \mathrm{curl}(\mathbf{c})). \tag{A.1}$$

By considering the power contribution from external and internal sources, the dissipation inequality is written as,

$$D = \int_{\partial V} \mathbf{t_f}.\dot{\mathbf{u}}\, da + \int_V \mathbf{b}.\dot{\mathbf{u}}\, dv - \frac{d}{dt}\int_V \psi\, dv - \frac{d}{dt}\int_V \frac{1}{2}\rho_o|\dot{\mathbf{u}}|^2\, dv, \tag{A.2}$$

where $\mathbf{t_f}, \mathbf{b}$ are the traction and body forces respectively. $\dot{\mathbf{u}}$ is the velocity field and ρ_o is the mass density. The first term in Eq. (A.2) can be modified as

$$\int_{\partial V} \mathbf{t_f}.\dot{\mathbf{u}}\ da\ = \int_{\partial V} \mathbf{T}\mathfrak{n}.\dot{u}\ da = \int_V \left(\dot{u}.div\mathbf{T} + \mathbf{T} : \text{grad}(\mathbf{V})\right)\ dv. \tag{A.3}$$

Substituting Eq. (A.3) in Eq. (A.2) and rearranging the terms

$$D = \int_V (div\mathbf{T} + \mathbf{b} - \rho_o\ddot{u}).\dot{u}\ dv + \int_V \mathbf{T} : grad(\mathbf{V})\ dv - \frac{d}{dt}\int_V \psi\ dv. \tag{A.4}$$

From the balance of linear momentum the first term in Eq. (A.4) becomes zero. Hence, the dissipation can be represented as

$$D = \int_V \mathbf{T} : \text{grad}(\mathbf{V})\ dv - \frac{d}{dt}\int_V \psi\ dv. \tag{A.5}$$

Upon substituting the free energy density function Eq. (A.1) in Eq. (A.5) the dissipation can be written as

$$D = \int_V \mathbf{T} : \text{grad}(\mathbf{V})\ dv - \frac{d}{dt}\int_V \psi(\boldsymbol{\varepsilon}^e, \mathbf{c}, \text{curl}(\mathbf{c}))\ dv. \tag{A.6}$$

By taking the time derivative inside the integral, Eq. (A.6) can be written as

$$D = \int_V \mathbf{T} : \text{grad}(\mathbf{V})\ dv - \int_V \left(\frac{\partial \psi}{\partial \boldsymbol{\varepsilon}^e}\ \dot{\boldsymbol{\varepsilon}}^e + + \frac{\partial \psi}{\partial \mathbf{c}}\ \dot{\mathbf{c}} + \frac{\partial \psi}{\partial \mathbf{t}}\ \dot{\mathbf{t}}\right)\ dv. \tag{A.7}$$

With elastic strain $\boldsymbol{\varepsilon}^e = \boldsymbol{\varepsilon} - \boldsymbol{\varepsilon}^p$, in Eq. (A.7)

$$D = \int_V \mathbf{T} : \text{grad}(\mathbf{V})\ dv - \int_V \left(\frac{\partial \psi}{\partial \boldsymbol{\varepsilon}^e}\ (\dot{\boldsymbol{\varepsilon}} - \dot{\boldsymbol{\varepsilon}}^p) + \frac{\partial \psi}{\partial \mathbf{c}}\ \dot{\mathbf{c}} + \frac{\partial \psi}{\partial \mathbf{t}}\ \dot{\mathbf{t}}\right)\ dv. \tag{A.8}$$

Utilizing Eq. (1) and rearranging the terms

$$\begin{aligned} D = \int_V (\mathbf{T} - \frac{\partial \psi}{\partial \boldsymbol{\varepsilon}^e}) : \text{grad}(\mathbf{V})\ dv + \int_V \frac{\partial \psi}{\partial \boldsymbol{\varepsilon}^e}\ \dot{\boldsymbol{\varepsilon}}^p\ dv - \int_V \frac{\partial \psi}{\partial \mathbf{c}}\ .(\mathbf{t} \times \mathbf{V})\ dv - \\ \int_V \frac{\partial \psi}{\partial \mathbf{t}}\ .(-\text{curl}(\dot{\mathbf{c}}))\ dv. \end{aligned} \tag{A.9}$$

The third term in Eq. (A.9) can be written as

$$\int_V \frac{\partial \psi}{\partial \mathbf{c}}\ .(\mathbf{t} \times \mathbf{V})\ dv = \int_V (\partial_{\mathbf{c}}\psi \times \mathbf{t}).\mathbf{V}. \tag{A.10}$$

Similarly, the fourth term in Eq. (A.9) can be modified as

$$\begin{aligned}\int_V \frac{\partial \psi}{\partial \mathbf{t}}.(\text{curl}(\dot{\mathbf{c}})) &= \int_V \dot{\mathbf{c}}.(\nabla \times \partial_{\mathbf{t}}\psi)\ dv - \int_{\partial v} (\partial_{\mathbf{t}}\psi \times \dot{\mathbf{c}})\ da \\ &= \int_V (\mathbf{t} \times \mathbf{V}).(\text{curl}(\partial_{\mathbf{t}}\psi))\ dv - \int_{\partial v} (\partial_{\mathbf{t}}\psi \times (\mathbf{t} \times \mathbf{V}))\ da \\ &= \int_V (\text{curl}(\partial_{\mathbf{t}}\psi) \times \mathbf{t}).\mathbf{V}\ dv + \int_{\partial v} \mathbf{V}.[(\partial_{\mathbf{t}}\psi \times \mathbf{n}) \times \mathbf{t}]\ da.\end{aligned} \tag{A.11}$$

Finally, substituting Eq. (A.10) and Eq. (A.11) in Eq. (A.9) the dissipation can be written as,

$$\begin{aligned}D = &\int_V (\mathbf{T} - \partial_{\boldsymbol{\varepsilon}^e}\psi) : \text{grad}(\mathbf{V})\ dv + \\ &\int_V \mathbf{T} : \dot{\boldsymbol{\varepsilon}^p}\ dv + \int_V \Big\{[-\partial_{\mathbf{c}}\psi + \text{curl}(\partial_{\mathbf{t}}\psi)] \times \mathbf{t}\Big\}.\mathbf{V}\ dv + \int_{\partial v} \mathbf{V}.[(\partial_{\mathbf{t}}\psi \times \mathbf{n}) \times \mathbf{t}]\ da.\end{aligned} \tag{A.12}$$